minerals

MDPI

Article

Partial Melting and Crustal Deformation during the Early Paleozoic Wuyi–Yunkai Orogeny: Insights from Zircon U-Pb Geochronology and Structural Analysis of the Fuhuling Migmatites in the Yunkai Region, South China

Junhao Zhang [1,2], Weiliang Liu [2,*], Chris Yakymchuk [3], Rina Sa [4], Zhen Zeng [5], Ruxin Ding [1], Gongjian Tang [6], Hanqi Liu [7], Qingyan Xu [1] and Yong Wang [1]

1 School of Earth Sciences and Engineering, Sun Yat-sen University, Guangzhou 510275, China; zhj247582447@163.com (J.Z.); dingrux@mail.sysu.edu.cn (R.D.); qingyanxu3@163.com (Q.X.); lavawangy@gmail.com (Y.W.)
2 School of Marine Sciences, Sun Yat-sen University, Guangzhou 510006, China
3 Department of Earth and Environmental Sciences, University of Waterloo, ON N2L 3G1, Canada; chris.yakymchuk@uwaterloo.ca
4 Guangzhou Marine Geological Survey, China Geological Survey, Guangzhou 510760, China; sarina_gmgs@163.com
5 China Aerospace Academy of Architectural Design and Research Co., Beijing 100162, China; zengzhen6301@163.com
6 State Key Laboratory of Isotope Geochemistry, Guangzhou Institute of Geochemistry, Chinese Academy of Sciences, Guangzhou 510640, China; tanggj@gig.ac.cn
7 Geophysical Exploration Center, China Earthquake Administration, Zhengzhou 450002, China; liuhq@gec.ac.cn
* Correspondence: liuweil@mail.sysu.edu.cn

Received: 28 August 2019; Accepted: 5 October 2019; Published: 9 October 2019

Abstract: Migmatites record crucial information about the rheology and tectonothermal evolutionof the deep crust during orogenesis. In the Wuyi–Yunkai orogen in South China, migmatites at Fuhuling record Early Paleozoic high temperatures and associated partial melting. However, the absolute timing and implications for the rheology of the deep crust during orogenesis are poorly constrained. In this contribution, we used spatial analysis of migmatitic leucosomes, structural analysis, and U-Pb geochronology of zircon to elucidate the absolute timing of crustal partial melting, the degree of partial melting, and the role of partial melting on the rheology of the crust during the Wuyi–Yunkai orogeny. Partial melting of the Fuhuling migmatites occurred at *c.* 440 Ma during Early Paleozoic Wuyi–Yunkai orogenesis. Subsequent lower temperature metamorphism associated with Indosinian movement that caused minor zircon recrystallization was temporally associated with the crystallization of nearby biotite monzogranites, but it did not influence the morphology of the Fuhuling migmatites. The migmatites preserve a morphological transition from metatexite to diatexite with an increasing proportion of leucosome. This transition preserves different structural characteristics that represent the response of the solid framework and melt network to variable melt fractions during partial melting. The large proportion of in situ or in source leucosome in the Fuhuling migmatites suggests that it was a melt-rich crustal horizon during orogenesis, and that a substantial proportion of anatectic melt was retained in the deep crust. The rheological transition documented in the Fuhuling migmatites was caused by changes in the melt fraction, and it is an analogue for the rheological transition characteristics of melt-rich crustal horizons in the Yunkai region during Early Paleozoic Wuyi–Yunkai orogenesis and subsequent orogenic collapse.

Keywords: metatexite; diatexite; crustal partial melting; rheological transitions; Wuyi–Yunkai orogeny

1. Introduction

Geological and geophysical studies in modern and ancient orogens demonstrate that the middle to lower continental crust can be partially molten during orogenesis [1–5]. Partial melting drastically weakens the crust and plays an essential role in the rheological evolution of orogenic systems [5–7]. Migmatites are rocks that have partially melted at high temperatures in the crust [5] and have two broad morphologies, metatexite and diatexite, based on increasing melt fraction and the continuity of the solid framework [8–11]. Metatexite generally preserves relict (i.e., pre-anatectic) structures and form as the melt is extracted from intergranular space and the solid framework fuses together [5,12,13]. Diatexite rarely preserves pre-partial melting structures, and it forms when the melt proportion increases to the extent that the solid framework is no longer connected, resulting in strengths close to that of magmas [14–16]. These two types of migmatites are structurally and compositionally heterogeneous, and they preserve deformation features that arise from rheological transitions related to melt-dominated to melt-absent behavior [5,11,17,18]. Therefore, migmatites act as an analogue for the rheological behavior of partially molten crust during orogenesis [8,10,19,20]. High-grade gneiss terranes typically undergo multiple deformation and metamorphic episodes, and, consequently, migmatites at the outcrop scale generally have complex geometries and structures that overprint the topology of the melt network that existed during crustal parting melting [10,19,20]. Migmatites can also be overprinted by brittle–ductile shear zones, which further complicates the interpretation of migmatitic structures [19,21]. Considering the complex geological history of most migmatites, detailed field mapping and structural analyses are needed to understand the anatectic melt network of migmatites [11,12,18,22–26] and are crucial for providing insights into the mechanics of melt production, melt segregation, melt migration, and melt redistribution during crustal partial melting accompanying orogenesis [8,10,11,27,28]. However, there is still a poor understanding of the relative roles of deformation versus melt fraction during the transition from metatexite to diatexite in migmatite terranes, but this information is crucial for linking structures in migmatites to the broader evolution of orogenic belts.

The Wuyi–Yunkai orogen is an intracontinental orogen (traditionally called the "Caledonian orogen" or "Kwangsian orogen" in Chinese literature [29–31]). The orogen covers the southeastern half of the South China block (Figure 1b), extends for ~2000 km in a northeasterly direction, and contains widespread migmatites formed by the partial melting of continental crust during the Early Paleozoic [29–31]. The Yunkai region is a crucial exposure of the deep crust that records Early Paleozoic crustal partial melting in the Wuyi–Yunkai orogen [29–32]. However, whether partial melting in the Yunkai region occurred in a single event or in multiple pulses is still debated [32–36]. Previous studies on migmatites in the Yunkai region focused on the timing and nature of partial melting on the evolution of the Wuyi–Yunkai orogen [30–32,37]. However, little work has been done on the relationships between crustal partial melting, rheological transitions, and structural transitions from metatexites to diatexites, which are all crucial for understanding the nature of partial melting that operated in the Wuyi–Yunkai orogeny and the broader significance of metatexite to diatexite transitions in migmatite terranes.

The Fuhuling migmatites in the Yunkai region are situated on the southwestern margin of the Wuyi–Yunkai orogen (Figure 2a) [38]. A complete metatexite–diatexite profile with distinct lithological changes and variations in migmatite morphology is exposed on the southeast coast. Therefore, the Fuhuling migmatites provide a rare opportunity to investigate the relationship between crustal partial melting, rheological transitions, and migmatite structures for the Yunkai region. Here, we present a detailed structural analysis of the migmatites as well as new zircon U-Pb geochronology and trace elements analysis from metatexite, diatexite, and biotite monzogranite in the Fuhuling region to

determine the timing of crustal partial melting and the implications for the tectonic evolution of the Yunkai region. In addition, detailed spatial and structural analysis of the Fuhuling migmatites is used to constrain the relationship of deformation versus melt fraction during the metatexite–diatexite transitions in migmatite terranes. Finally, using the Fuhuling migmatites as an analogue for the deep crust coupled with the results of U-Pb zircon geochronology, we discuss the rheological transition that occurred during crustal partial melting in the Yunkai region during Early Paleozoic Wuyi–Yunkai orogeny.

2. Geological Setting

2.1. Regional Geology

The South China block (SCB) consists of the Yangtze Block in the northwest and the Cathaysia Block in the southeast. The present boundary between these two blocks in eastern South China is the approximately NE-trending Jiang-Shao Fault, but the extension of this boundary in the southwestern SCB is uncertain because of its poor exposure and younger tectonic overprinting [31,39]. The Wuyi–Yunkai orogen covers the southeastern half of the SCB, stretches for ~2000 km in a northeasterly direction, and is unconformable with Devonian strata [29,31]. Metamorphic rocks in the orogen are Paleozoic and older and are intruded by granites with crystallization ages mostly between 464 and 400 Ma ([40] and reference therein). The Yunkai region is a part of the Wuyi–Yunkai orogen and is located in the western Cathaysia block (Figure 1a). The metamorphosed basement in the Yunkai region is mainly composed of the Gaozhou Complex and Yunkai Group, which are unconformably overlain by weakly metamorphosed to unmetamorphosed Cambrian to Devonian strata (Figure 2a) [31,37,41,42]. The Gaozhou Complex is composed of amphibolite facies (locally granulite facies) paragneiss, schist, quartzite, marble, and migmatites, whereas the Yunkai Group is composed of lower-grade schist, slate, and phyllite as well as less common paragneiss, amphibolite, and marble [34,37]. Late Paleozoic to Cenozoic sedimentary rocks and Paleozoic to Early Mesozoic granites also occur in the Yunkai region (Figure 2a) [41–43].

Fuhuling is located in Yangxi County of Yangjiang City in Guangdong Province on the edge of the South China Sea (Figure 2a). It is tectonically situated in the southeastern margin of the Yunkai region (Figure 2a) [38]. The topography of Fuhuling is dominated by a peninsula-like hill surrounded by seas and covered with vegetation; it has a maximum elevation of 138 m above sea level. The dominant rock type in Fuhuling is migmatite, which includes metatexite and diatexite varieties [38]. Here, metatexite defines a migmatite where gneissic banding is evident, and diatexite contains no continuous gneissic banding (e.g., [14]). Neoproterozoic–Early Paleozoic metasedimentary rocks mainly consist of metagreywacke and biotite-quartz schist [38,44,45] that outcrop on the top and the hillside of Fuhuling (Figure 2b). A small area of biotite monzogranite is exposed on the southwestern beach of Fuhuling (Figure 2b) [38].

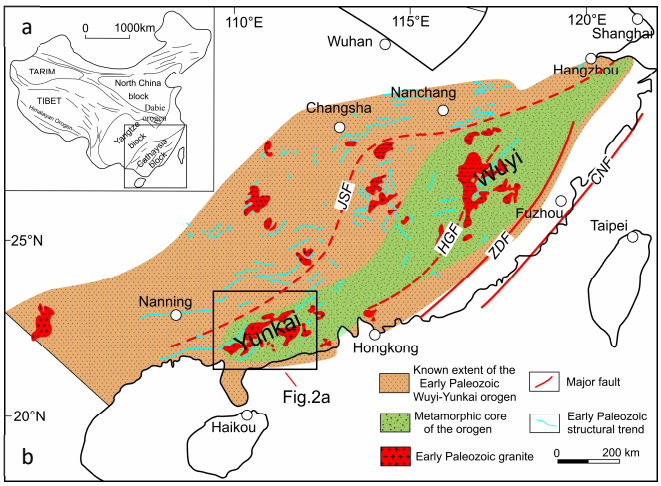

Figure 1. (**a**) Geological map of China (modified after [46]). (**b**) Simplified regional map with highlighted regions showing the Early Paleozoic Wuyi–Yunkai orogen; JSF = Jiangshan–Shaoxing fault; HGF = Heyuan–Guangfeng fault; ZDF = Zhenghe–Dapu fault; CNF = Changle–Nanao fault (modified after [30,31,41,47]).

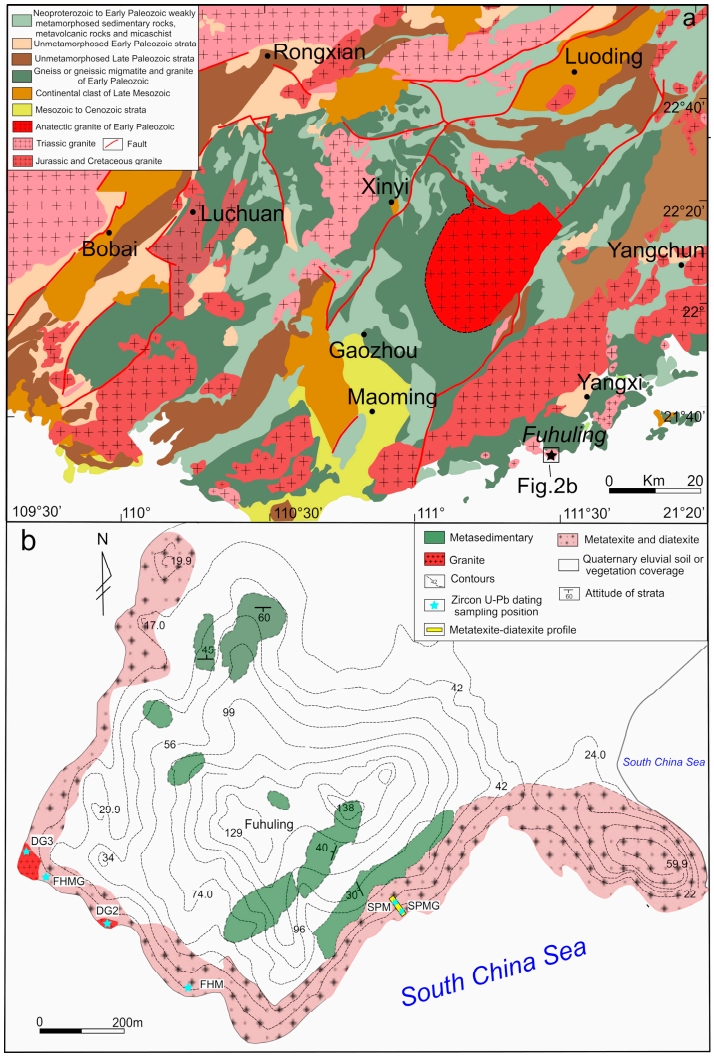

Figure 2. (**a**) Geological map of the Yunkai region (modified after [31,41]). (**b**) Geological map of Fuhuling with the metatexite–diatexite profile and sampling locations for U-Pb zircon geochronology.

2.2. Outcrop-Scale Structure

Metatexite and diatexite are only exposed on cliffs and beaches along the coast of Fuhuling [38]. There is a complete vertical metatexite–diatexite profile (<15 m in height) exposed in the southeastern portion of the research area (Figures 2 and 3). Based on compositional and structural variations, we divided this profile into four layers from top to bottom (Figure 3). Below, we use the terms leucosome to refer to the light-colored portion of a migmatite and melanosome for the dark-colored portion [14].

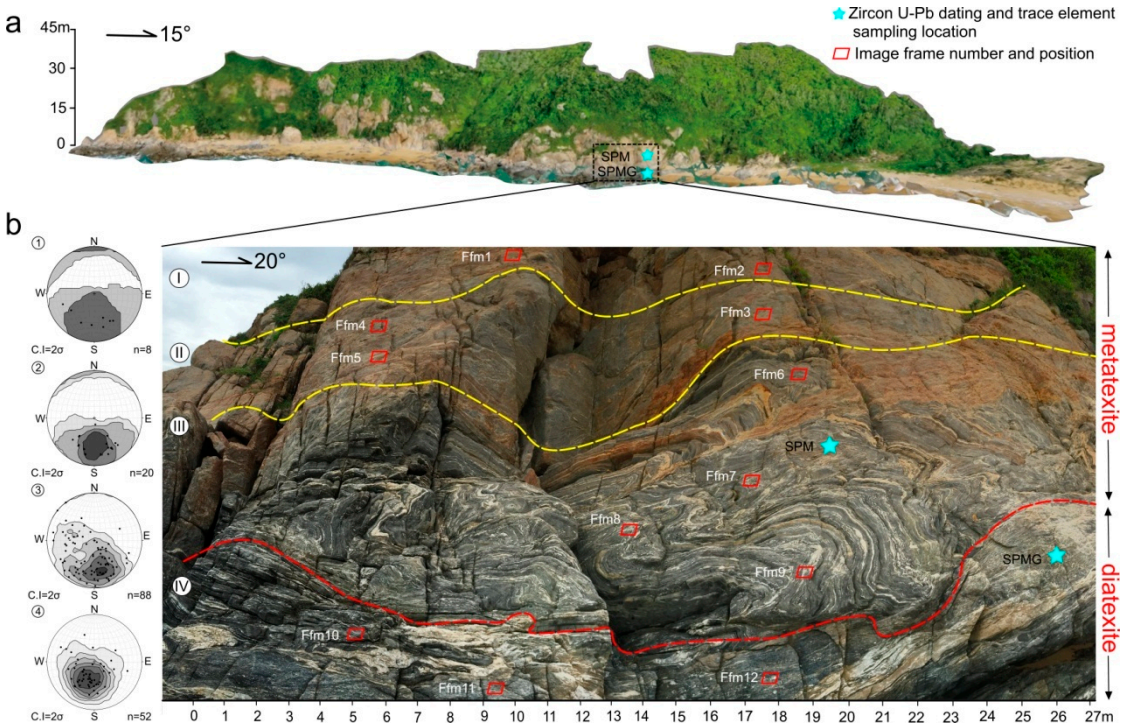

Figure 3. Profile of the Fuhuling metatexite–diatexite transition. (**a**) 3D image of the beach at the southeast of Fuhuling taken by an unmanned aerial vehicle. The location of the metatexite–diatexite profile is marked by the black dashed line box, and the sampling positions for zircon U-Pb geochronology are marked by stars. (**b**) Metatexite–diatexite profile in which the yellow and red dashed lines are boundaries between layer I, layer II, layer III, and layer IV. Red boxes mark the position of leucosome proportion measurements and are numbered by Ffm1–12. Stars mark the positionsof samples for zircon U-Pb geochronology. ①, ②, ③, and ④ on the left are the layer I, II, III, and IV stereonets of structural data, which show changes in leucosome orientations from metatexite to diatexite. Kamb contours of the structural data are shown with 2σ contour intervals. The software Stereonet version 6.3.3 by Richard Allmendinger was used for the equal-area stereographic projections. (http://www.geo.cornell.edu/geology/faculty/RWA/programs.html).

Layer I is a metatexite with ~5 area % (inferred to be equivalent to vol. %) of leucosome, which occurs as elongate lenses (<1 cm in diameter) and intermittent stroma (<2 mm in thickness; Figure 4a). These are typical stromatic structures of metatexite [25]. The orientations of eight stromatic leucosomes have poles between 150° to 252° with dips of 29° to 54° (Figure 3).

Layer II is also a stromatic metatexite but with a larger proportion (~10 area %) of leucosome compared to that of Layer I. Leucosomes in Layer II generally occur as stroma <2 cm thick, and some are slightly bent (Figure 4b). The orientations of 20 stromatic leucosomes have poles between 139° and 225° with dips of 20–79° (Figure 3).

Layer III is a metatexite with folded leucosomes that change in wavelength and amplitude over short distances. Folds vary in morphology and include asymmetric, tight, ptygmatic, parasitic, rootless,

and superimposed folds (Figure 4c,d). Leucosomes and melanosomes are thicker in fold hinges than in fold limbs. In the lower part of layer III, metatexite is in transitional contact with diatexite and has fewer stromatic leucosomes (Figure 4g). Stromatic leucosomes have variable orientations; eighty-eight orientation measurements yield variable poles that are mostly 104° to 241° (Figure 3).

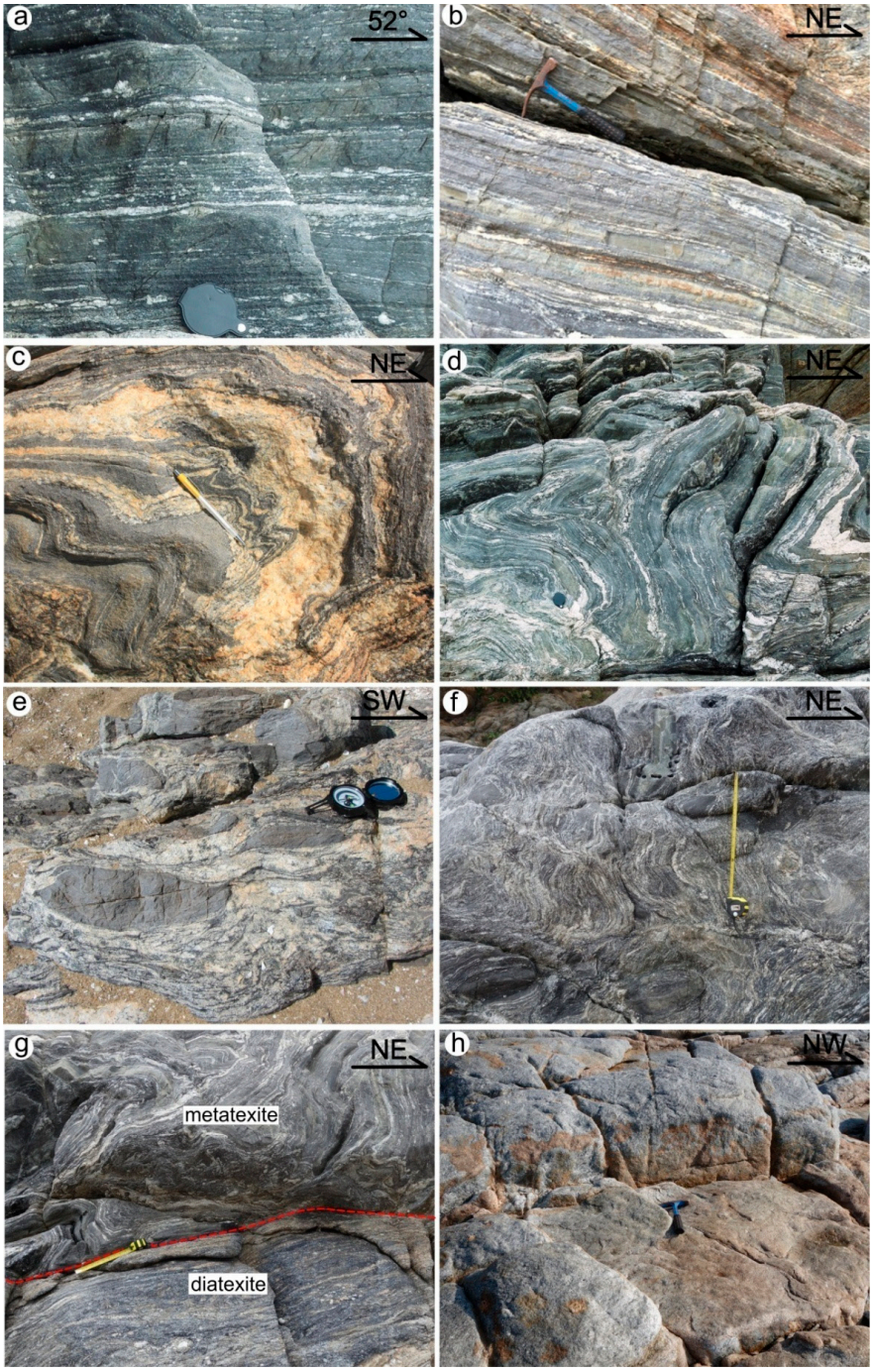

Figure 4. Representative field photographs of the Fuhuling metatexite, diatexite, and biotite monzogranite. (**a**) Approximately parallel orientation of leucosome stroma in metatexites. (**b**) Parallel orientation of leucosome in metatexites. (**c**,**d**) Variety of folds in the metatexite, for example, ptygmatic folds and superimposed folds in (**c**), rootless folds and tight folds in (**d**). (**e**) Schollen-structured diatexite with lenticular augen of paleosome or melting melanosome. (**f**) Schlieren-structured diatexite with leucosome layers 2–5 mm thick and slightly deformed paleosome blocks. (**g**) Contact between metatexite and diatexite. (**h**) Biotite monzogranite from Fuhuling.

Layer IV is a diatexite, and leucosomes and melanosomes in this layer mainly form schollen structures as well as schlieren and nebulitic structures(Figure 4d,e). In the diatexite, there are some lenticular, hook-like, and trailing paleosomes (i.e., unmelted rock) or restites (i.e., melt-depleted residues) wrapped by leucosome (Figure 4f). The diatexite exhibits schollen structures as well as schlieren and nebulitic structures (Figure 4d,e) [18,48]. The orientation of fifty-two leucosomes have poles between 61° to 354° with dips of 24° to 85°, and there is no significant directionality (Figure 3).

2.3. Petrology and Microstructure

Metatexites have a medium- to coarse-grained granular textures. Melanosomes are composed of plagioclase (~35 vol.%), K-feldspar (~30 vol.%), quartz (~20 vol.%), and biotite (~15 vol.%) with accessory apatite, zircon, monazite, Fe-Ti oxides, and allanite. Fine-grained quartz is interstitial to K-feldspar, plagioclase, and coarser-grained quartz. Boundaries between quartz and other main minerals vary from lobate or straight. The size of plagioclase and K-feldspar varies from 0.8 to 3 cm. Plagioclase andK-feldspar have microfractures (Figure 5a) which may be filled with fine-grained, drop-shaped quartz (Figure 5b).Some coarse-grained quartz shows undulatory extinction (Figure 5c). Fine-grained biotite (0.05–0.4 mm) has straight boundaries with K-feldspar, plagioclase, and quartz. Quartz also forms "string of beads" [49] microstructures that are interstitial to K-feldspar, plagioclase, and quartz (Figure 5d).

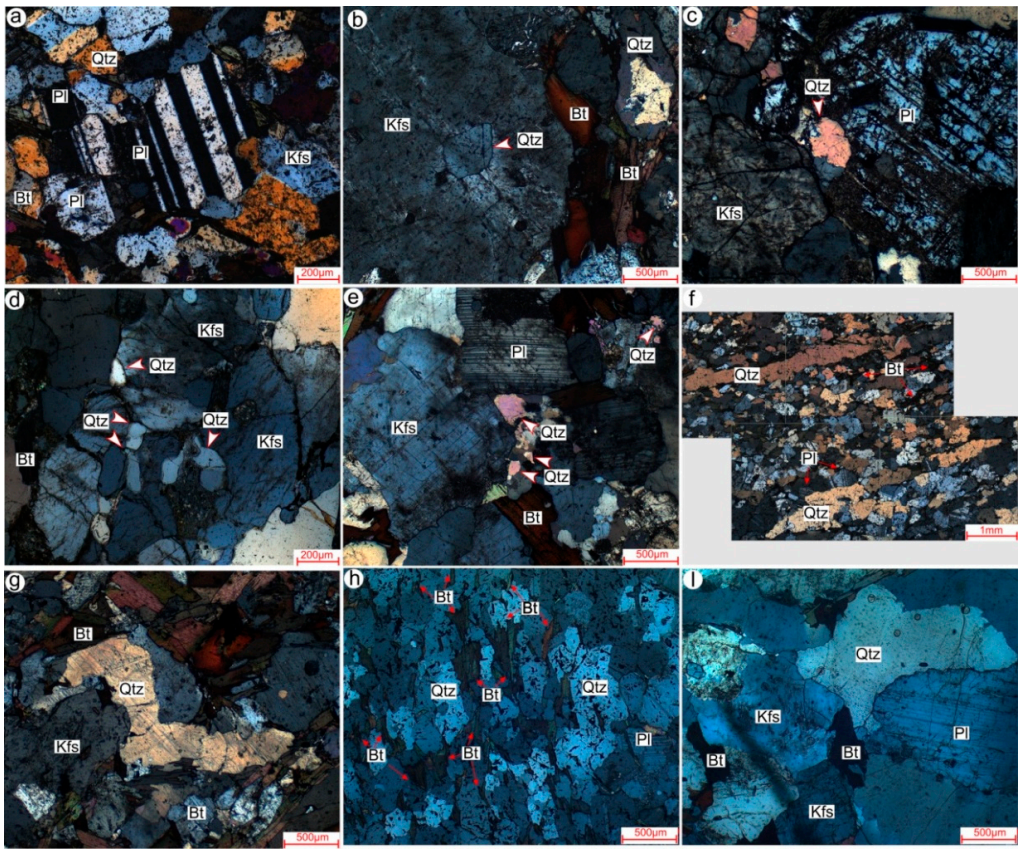

Figure 5. Microstructures of the Fuhuling metatexite, diatexite, and biotite monzogranite. (**a**) Microcracks in plagioclase in the metatexite. (**b**,**c**) Interstitial quartz at grain boundaries or within microcracks of K-feldspar in metatexites (arrows). (**d**) String of beads microstructure interstitial to quartz, K-feldspar, and plagioclase in the metatexite. (**e**) Interstitial quartz at triple junctions in diatexites (arrows). (**f**) Elongate quartz in the diatexite. (**g**) "Zig-zag type" quartz in the diatexite. (**h**) Oriented fine-grained biotite in the diatexite. (**i**) Representative photomicrograph of the medium- to coarse-grained biotite monzogranite. All photos are in crossed-polarized light. Abbreviations: Qtz—quartz; Kfs—K-feldspar; Pl—plagioclase; Bt—biotite.

Diatexites have a medium- to coarse-grained granular texture. Melanosomes contain plagioclase (~35 vol.%), K-feldspar (~30% vol.%), quartz (~25 vol.%), and biotite (~10 vol.%) with minor amounts of hornblende, sillimanite, apatite, zircon, Fe-Ti oxides, and allanite. Quartz is interstitial to plagioclase and K-feldspar (Figure 5e), but it is locally elongate and shows "zig-zag type" microstructures (Figure 5f,g). Quartz has lobate to straight boundaries with K-feldspar and plagioclase and also displays undulatory extinction. Biotite is fine-grained (0.05–0.5 mm in diameter), is oriented parallel to elongate quartz (Figure 5h), and has straight boundaries with K-feldspar, plagioclase, and quartz. Some fine-grained (0.05–0.2 mm) biotite is interstitial to K-feldspar, plagioclase, and quartz.

The metatexites and diatexites both contain abundant leucosomes (Figure 3). Leucosomes in both metatexites and diatexites are composed of plagioclase (~40 vol.%), K-feldspar (~30 vol.%), quartz (~25 vol.%), and biotite (~5 vol.%) with accessory apatite, zircon, monazite, Fe-Ti oxides, and allanite.

Biotite monzogranites are medium- to coarse-grained and contain plagioclase (~35 vol.%), K-feldspar (~30 vol.%), quartz (~30 vol.%), and biotite (~5 vol.%) with accessory apatite, zircon, xenotime, Fe-Ti oxides, and allanite. Quartz is anhedral to euhedral with straight to lobate boundaries. Biotite varies in size with some fine-grained biotite interstitial to K-feldspar, plagioclase, and quartz. Plagioclase is subhedral to euhedral with minor deformation twins and undulatory extinction (Figure 5f).

3. Sample Selection and Analytical Methods

Six samples from Fuhuling were selected for zircon U-Pb geochronology and trace element analysis, including two metatexite samples (sample No.: SPM and FHM), two diatexite samples (sample No.: SPMG and FHMG), and two biotite monzogranite samples (sample No.: DG2 and DG3). SPM and SPMG were collected from layer III and layer IV of the metatexite–diatexite profile, respectively. FHM, FHMG, DG2, and DG3 were all collected from the southwestern beach of Fuhuling (Figure 2).

Zircon separation and cathodoluminescence (CL) imaging were both completed by the Honesty Geological Service Company in Langfang, Hebei Province. The CL images were acquired using a JSM6510 (Japan) scanning electron microscope fitted with a GatanMini CL detection system. LA-ICPMS zircon U-Pb isotopic dating and trace element analyses were synchronously carried out using an Agilent 7500a ICP-MS coupled with a GeoLas2005 laser ablation system at the State Key Laboratory of Geological Processes and Mineral Resources, China University of Geosciences (Wuhan). Laser ablation was conducted with a beam diameter of 32 μm for all analyses. Each analysis incorporated an approximately 20 s background acquisition (i.e., gas blank) followed by 50 s of ablation. The software ICPMSDataCal was used to perform off-line selection and integration of background and analyte signals, time-drift corrections, quantitative calibration for trace element analyses, and U-Pb geochronology [50,51]. Specific analytical conditions are detailed in Liu et al. (2010) [51]. Common Pb corrections were undertaken using ComPbCorr#3_17 of Andersen (2002) [52]. Count rates for ^{29}Si, ^{204}Pb, ^{206}Pb, ^{207}Pb, ^{208}Pb, ^{232}Th, and ^{238}U were collected for age determination. Trace element compositions of zircon were calibrated against NIST SRM 610 and using Si as an internal standard; analytical accuracies are generally better than 5–10% for trace elements [50]. Zircon weighted mean ages and U-Pb concordia diagrams were calculated with the software ISOPLOT (version 3.0) [53]. Uncertainties on individual LA-ICPMS analyses were reported at the 1σ level, and uncertainties on weighted mean ages were quoted at a level of confidence of 95% (2σ). Given the low abundance of ^{207}Pb in young zircon, we used ^{206}Pb/^{238}U ages to calculate weighted mean ages for zircon <1000 Ma, and ^{207}Pb/^{206}Pb ages were preferentially adopted for zircons for >1000 Ma. We excluded zircon U-Pb analyses with discordance values >10% for inherited zircon cores and >5% for metamorphic zircon and magmatic zircon from weighted mean ages, histograms, density probability plots, and U-Pb concordia diagrams. The complete data set, including the excluded discordant analyses, is reported in Supplementary Table S1.

4. Results

4.1. Zircon U-Pb Geochronology

Cathodoluminescence images of representative zircons together with spot ages are shown in Figure 6. U-Pb data for these samples are summarized on Wetherill concordia diagrams in Figure 7.

Figure 6. Representative cathodoluminescence (CL) images of analyzed zircons from metatexite samples (SPM, FHM), diatexite samples (SPMG, FHMG), and biotite monzogranite samples (DG2, DG3) samples in Fuhuling. Red circles show LA-ICPMS dating spots in inherited zircon of discordance values <10%, metamorphic zircon and magmatic zircon of discordance values <5%, and corresponding U-Pb ages. Yellow circles show LA-ICPMS dating spots in metamorphic zircon and magmatic zircon of discordance values >5%.

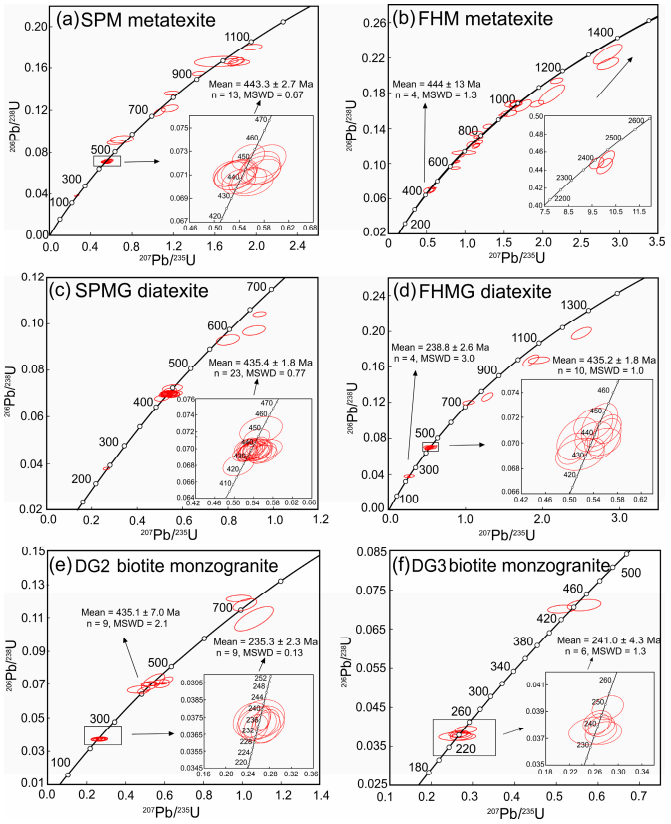

Figure 7. Zircon LA-ICPMS U-Pb concordia diagrams for the samples of Fuhuling with uncertainties on the weighted-mean ages are reported at 2σ. (**a**) metatexite sample (SPM) and discussed zircon spots. (**b**) metatexite sample (FHM) and discussed zircon rims. (**c**) diatexite sample (SPMG) and discussed zircon spots. (**d**) diatexite sample (FHMG) and discussed zircon spots. (**e**) biotite monzogranite sample (DG2) and discussed zircon spots. (**f**) biotite monzogranite sample (DG2) and discussed zircon spots. See the text for a detailed explanation.

4.1.1. Metatexite

Zircon from metatexite SPM was long or short prismatic, subhedral to euhedral, and had lengths of 50–200 μm. CL images revealed that most zircon had distinct cores and rims. Cores exhibited weak oscillatory, planar, or nebulous zoning, and the rims showed weak oscillatory zoning or no zoning (Figure 6) [54,55]. Thirty-nine spots were analyzed from 39 zircon grains. Eleven analyses of inherited cores showed a range of ages from 553 ± 8 to 1278 ± 402 Ma (Table S1). Twenty-eight analyses were conducted on zircon rims. Four of these analyses yielded $^{206}Pb/^{238}U$ ages that ranged from 238 ± 4 to 245 ± 3 Ma and two analyses (20r, 38r) with >5% discordance; the remaining 2 analyses (4r, 31r) had $^{206}Pb/^{238}U$ ages of 244 ± 4 and 240 ± 2 Ma, respectively. The other 24 of the 28 analyses yielded $^{206}Pb/^{238}U$ ages of 434 ± 4 to 454 ± 5 Ma. After excluding 11 analyses with discordances >5%, the remaining 13 concordant ones yielded a weighted mean of 443.3 ± 2.7 Ma (mean squared weighted deviates (MSWD) = 0.67) (Figure 7a).

Zircon from metatexite FHM was rounded or prismatic, subhedral, and ranged from 50 to 130 μm in length. Zircon was dark under CL and had core–rim structures. The cores exhibited weak oscillatory, planar, or nebulous zoning, and the rims showed no zoning or weak oscillatory zoning (Figure 6). Thirty-five spots were analyzed from 35 zircon grains. Twenty-eight analyses of cores yielded a range of ages from 585 ± 6 to 2480 ± 32 Ma (Table S1). Seven analyses of zircon rims yielded $^{206}Pb/^{238}U$ ages that ranged from 432 ± 13 to 448 ± 4 Ma. After excluding three analyses (4r, 15r, 28r) with discordance values>5%, the remaining four (3r, 13r, 25r, 30r) analyses formed a coherent group witha weighted mean $^{206}Pb/^{238}U$ age of 444 ± 13 Ma (MSWD = 1.6) (Figure 7b).

4.1.2. Diatexite

Zircon from diatexite SPMG was mainly subhedral to euhedral, long prismatic, and 70 to 200 μm long. CL images revealed that there were two types of zircon. One type had core–rim structures; cores exhibited oscillatory, planar, or nebulous zoning, whereas rims showed weak oscillatory zoning or were unzoned (Figure 6). The second type of zircon was dark under CL and had homogeneous internal structures with weak or no oscillatory zoning. Thirty-eight spots were analyzed from 38 zircon grains in SPMG. Three analyses of inherited cores yielded $^{206}Pb/^{238}U$ ages between 573 ± 9 to 639 ± 4 Ma (Table S1). Of the thirty-five analyses on rims of zircons with core–rim structures or on homogeneous zircon, one analysis had a $^{206}Pb/^{238}U$ age of 240 ± 3 Ma, and the other 34 analyses yielded $^{206}Pb/^{238}U$ ages between 424 ± 5 to 454 ± 5 Ma. After eliminating 11 analyses with discordance values >5%, the other 23 yielded a weighted mean $^{206}Pb/^{238}U$ age of 435.4 ± 1.8 Ma (MSWD = 0.77) (Figure 7c).

Zircon from diatexite FHMG was mainly subhedral to euhedral and prismatic with lengths ranging from 70 to 180 μm. Under CL, most zircons had core–rim structures, and the cores exhibited oscillatory, planar, or nebulous zoning, whereas the rims showed weak oscillatory zoning or no zoning (Figure 6); some zircon was internally homogeneous with weak or no oscillatory zoning. Twenty-four spots were analyzed from 24 zircon grains in FHMG. Five analyses of inherited cores yielded ages ranging from 730 ± 9 to 1503 ± 181 Ma (Table S1). Nineteen analyses were conducted on rims of zircon with core–rim structures or on homogeneous zircons. Of these, six analyses showed a range of $^{206}Pb/^{238}U$ ages from 235 ± 3 to 243 ± 3 Ma. Two analyses (6h, 19h) with discordance values >5% were excluded, and the remaining four analyses (3r, 7r, 9r, 22r) yielded a weighted mean $^{206}Pb/^{238}U$ age of 238.8 ± 2.6 Ma (MSWD = 0.97).The other 13 analyses yielded $^{206}Pb/^{238}U$ ages ranging from 431 ± 5 to 448 ± 4 Ma. Excluding three discordant analyses(4h, 15r, 21r), the remaining 10 analyses yielded a weighted mean $^{206}Pb/^{238}U$ age of 437.5 ± 3.0 Ma (MSWD = 1.0) (Figure 7d).

4.1.3. Biotite Monzogranite

Zircon from biotite monzogranite DG2 was mainly long or short prismatic, subhedral to euhedral, with lengths of 50 to 200 μm. In CL images, most zircon had no inherited cores, was dark under CL, and exhibited weak oscillatory zoning. Some zircon showed core–rim structures with oscillatory-zoned cores, whereas rims exhibited weak oscillatory zoning or no zoning (Figure 6). Twenty-nine spots were analyzed from 29 zircon grains. Nine of 12 analyses of cores had $^{206}Pb/^{238}U$ ages of 413 ± 8 to 449 ± 9 Ma with a weighted average of 435.1 ± 7.0 Ma (MSWD = 2.1), and the other 3 analyses yielded $^{206}Pb/^{238}U$ ages of 670 ± 28, 718 ± 14, and 741 ± 7 Ma. The other 17 of 29 analyses were on oscillatory zones and gave $^{206}Pb/^{238}U$ ages between 233 ± 3 to 252 ± 5 Ma. After excluding eight analyses with discordance values of >5%, the remaining nine analyses yielded a weighted mean $^{206}Pb/^{238}U$ age of 235.3 ± 2.3 Ma (MSWD = 0.13)(Figure 7e), which is interpreted as the timing of magmatic crystallization.

Zircon from biotite monzogranite DG3 was mainly long or short prismatic, subhedral to euhedral, and had lengths of 50 to 220 μm. Most zircon had no inherited cores, was dark under CL, and had strong to weak oscillatory zoning; some zircons showed core–rim structures with oscillatory-zoned cores and rims with weak oscillatory zoning (Figure 6). Nineteen spots were analyzed from 19 zircon grains. Of three analyses of cores, one yielded a $^{207}Pb/^{206}Pb$ age of 1128 ± 69 Ma, and the other two analyses gave $^{206}Pb/^{238}U$ ages of 437 ± 4 and 443 ± 6 Ma (Table S1). The other 16 analyses on oscillatory zones yielded $^{206}Pb/^{238}U$ ages ranging from 234 ± 3 to 255 ± 4 Ma. After excluding ten analyses with discordance values >5%, the remaining six concordant analyses yielded a weighted mean $^{206}Pb/^{238}U$ age of 241.0 ± 4.3 (MSWD = 1.3)(Figure 7f), which is interpreted as the crystallization age of the biotite monzogranite.

4.1.4. Summary of U-Pb Zircon Ages from Migmatites

Analyses of inherited cores in zircon from migmatites had a wide range of ages (*c.* 2480–553 Ma) with the largest population at *c.* 1000 Ma. This is distinctly different from the age of inherited zircons from the biotite monzogranites, which ranged from *c.* 413 to 1128 Ma with the largest population at *c.* 440 Ma. U-Pb ages of metamorphic zircon from migmatites were mainly Caledonian in age, but some Indosinian ages were similar to the timing of biotite monzogranite crystallization. CL images showed that the metamorphic zircon had core–rim or homogeneous zoning, which indicates that they had undergone different degrees of resorption and recrystallization [54–56]. Therefore, zircon from the Fuhuling migmatites recorded metamorphic zircon growth during both the Caledonian and Indosinian.

4.2. Zircon Trace Elements

4.2.1. Metatexite

Trace element data of 39 analyses of 39 zircon grains from sample SPM are shown in Table S2, with 11 on inherited cores and the remaining 28 on rims. The inherited cores had high concentrations of Th (72–1092 ppm) and U (336–1842 ppm) with a wide range of Th/U ratios (0.045–1.49). Chondrite-normalized rare earth element (REE) patterns were characterized by steep heavy rare earth element (HREE) slopes ($(Yb/Gd)_N$ = 6.50–78.5, average = 20.4), positive Ce anomalies (Ce/Ce* = 1.31–85.0, average = 34.5), and prominent and negative Eu anomalies (Eu/Eu* = 0.0051–0.47, average = 0.16)(Figure 8a). Of the 28 rim analyses, four analyses with concordant $^{206}Pb/^{238}U$ ages of 238 ± 4 to 245 ± 3 Ma had a wide range of concentrations of Th (2–1411 ppm), with high U contents (251–4528 ppm), and a wide range of Th/U ratios (0.0068–0.97). Chondrite-normalized REE patterns were characterized by less steep HREE slopes ($(Yb/Gd)_N$ = 9.80–24.5), positive Ce anomalies (Ce/Ce* = 4.08–22.2), and significantly negative Eu anomalies (Eu/Eu* = 0.057–0.26) (Figure 8a). The remaining 24 analyses of zircon rims with concordant $^{206}Pb/^{238}U$ ages of 434 ± 4 to 454 ± 5 Ma yielded Th/U ratios of 0.14 to 0.73. Chondrite-normalized REE patterns were characterized by distinct and steep HREE slopes ($(Yb/Gd)_N$ = 10.8–37.8), prominent positive Ce anomalies (Ce/Ce* = 1.16–142, average = 37.0), and negative Eu anomalies (Eu/Eu* = 0.036–0.38) (Figure 8a).

For sample FHM, 28 analyses of inherited cores yielded high concentrations of U (278–5294 ppm) and Th (87–4366 ppm) with variable Th/U ratios (0.028–1.63). They displayed significant HREE enrichment ($(Yb/Gd)_N$ = 5.82–132, average = 28.0), prominent positive Ce anomalies with Ce/Ce* = 1.34–88.2 (average = 20.9), and negative Eu anomalies with Eu/Eu* = 0.010–1.15 (average = 0.26) on chondrite-normalized REE patterns, except for one analysis that had a positive Eu anomaly with Eu/Eu* = 1.15 (Figure 8b). Seven analyses of zircon rims had high concentrations of Th (60–965 ppm) and U (742–10664 ppm) with variable Th/U ratios of 0.070 to 0.56. Chondrite-normalized REE patterns were characterized by distinct and steep HREE slopes ($(Yb/Gd)_N$ = 12.5–40.7), positive Ce anomalies (Ce/Ce* = 1.44–18.8), and significantly negative Eu anomalies (Eu/Eu* = 0.001–0.69, average = 0.26) (Figure 8b).

4.2.2. Diatexite

For sample SPMG, three analyses of inherited cores had high concentrations of U (850–2873 ppm) and Th (214–369 ppm) with Th/U ratios of 0.023 to 0.25. Chondrite-normalized REE patterns were characterized by steep HREE slopes ($(Yb/Gd)_N$ = 31.4–42.4), positive Ce anomalies (Ce/Ce* = 2.84–18.9), and significantly negative Eu anomalies (Eu/Eu* = 0.086–0.20) (Figure 8c). One analysis of a rim with a $^{206}Pb/^{238}U$ age of 240 ± 3 Ma had a Th concentration of 49 ppm and a high U content of 2141 ppm with a Th/U ratio of 0.023. This analysis yielded a flat, chondrite-normalized HREE slope ($(Yb/Gd)_N$ = 12.0), positive Ce anomaly (Ce/Ce* = 7.69), and a negative Eu anomaly (Eu/Eu* = 0.041) (Figure 8c). Thirty-four analyses of zircon rims with concordant $^{206}Pb/^{238}U$ ages of 424 ± 5 to 454 ± 5 Ma yielded high concentrations of Th (94–1318 ppm) and U (578–4290 ppm) with Th/U ratios of 0.030 to 0.36. Chondrite-normalized REE patterns were characterized by steep HREE slopes

$((Yb/Gd)_N$= 3.08–81.5, average = 48.2), prominent and positive Ce anomalies (Ce/Ce* = 1.16–79.9, average = 12.5), and significantly negative Eu anomalies (Eu/Eu* = 0.002–0.21) (Figure 8c).

For sample FHMG, five analyses of inherited cores had high concentrations of Th (158–603 ppm) and U (460–1240 ppm) with Th/U ratios of 0.37 to 0.63. Chondrite-normalized REE patterns had steep HREE slopes ($(Yb/Gd)_N$ = 11.4–30.8), positive Ce anomalies (Ce/Ce* = 3.54–31.2), and negative Eu anomalies (Eu/Eu* = 0.18–0.38) (Figure 8d); these geochemical features are consistent with those measured in magmatic zircon [56,57]. Six of 19 analyses of homogeneous zircons and rims of zircons with core–rim structures had concordant $^{206}Pb/^{238}U$ ages of 235 ± 3 to 243 ± 3 Ma and yieldedvariable concentrations of Th (67–4015 ppm) and U (136–2161 ppm) and a large range of Th/U ratios (0.11–1.92). Chondrite-normalized REE patterns of these six analyses were characterized by flat HREE slopes ($(Yb/Gd)_N$ = 1.00–10.8), prominent and positive Ce anomalies (Ce/Ce* = 28.5–155), and negative Eu anomalies (Eu/Eu* = 0.057–0.73, average = 0.23) (Figure 8d). The remaining 13 analyses with concordant $^{206}Pb/^{238}U$ ages of 431 ± 5 to 448 ± 4 Mahad high concentrations of Th (154–1824 ppm) and U (431–2691 ppm) as well as Th/U ratios that varied from 0.14 to 1.20. Chondrite-normalized REE patterns were characterized by distinct and steep HREE slopes ($(Yb/Gd)_N$ =13.1–49.5), positive Ce anomalies (Ce/Ce* = 1.17–35.7), and prominent and negative Eu anomalies (Eu/Eu* = 0.015–0.31) (Figure 8d).

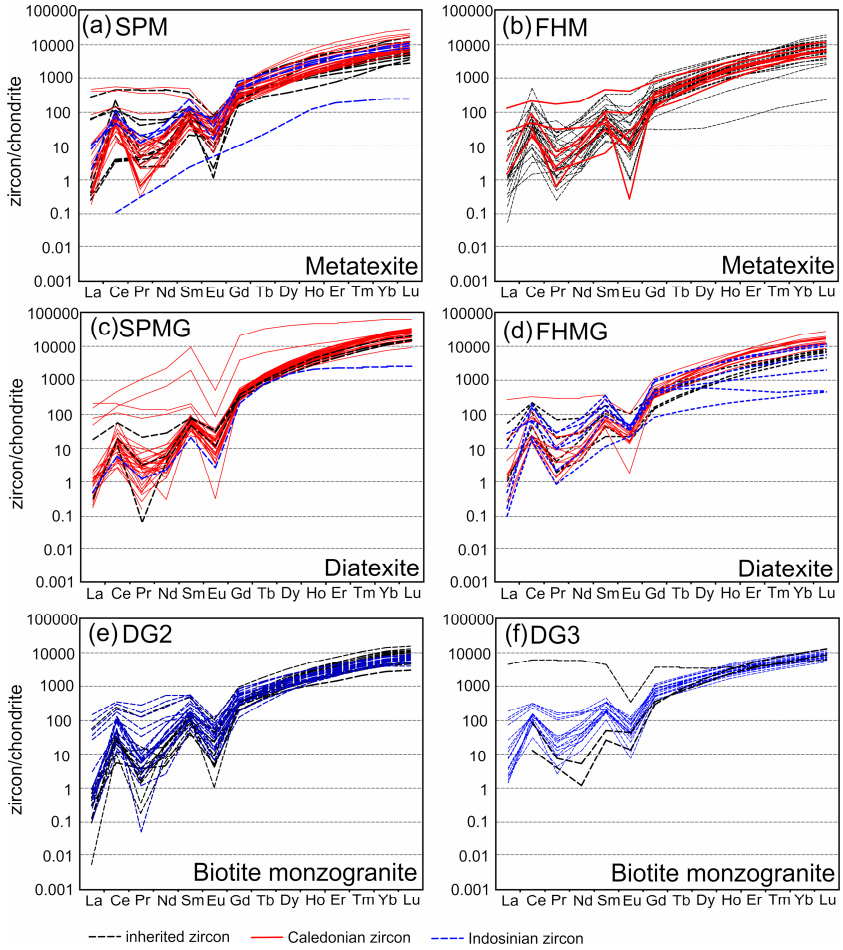

Figure 8. Chondrite-normalized REE patterns of zircons from samples of Fuhuling. (**a**) metatexite sample (SPM). (**b**) metatexite sample (FHM). (**c**) diatexite sample (SPMG). (**d**) diatexite sample (FHMG). (**e**) biotite monzogranite sample (DG2). (**f**) biotite monzogranite sample (DG3). The black dotted line represents the inherited zircon cores, the red line represents the early Paleozoic zircon and the blue dotted line represents the Indosinianzircon. Chondrite values are from [58].

4.2.3. Biotite Monzogranite

For sample DG2, 12 analyses were conducted on inherited cores, and 9 of these had $^{206}Pb/^{238}U$ ages ranging from 413 ± 8 to 449 ± 9 Ma, with high concentrations of U (389–1377 ppm) and Th (156–1309 ppm) yielding high Th/U ratios (0.26–1.00). Chondrite-normalized REE patterns were characterized by steep HREE slopes ($(Yb/Gd)_N$ = 14.7–35.9), prominent and positive Ce anomalies (Ce/Ce* = 2.97–331, average = 76.7), and significantly negative Eu anomalies (Eu/Eu* = 0.005–0.28) (Figure 8e). The other 3 of the 12 analyses yielded Th concentrations of 145, 217, and 340 ppm and U concentrations of 1166, 996, and 575 ppm, with Th/U ratios of 0.12, 0.22, and 0.59. Chondrite-normalized REE patterns were characterized by steep HREE slopes ($(Yb/Gd)_N$ = 14.4, 12.7, 15.1), positive Ce anomalies (Ce/Ce* = 5.3, 13.2, 68.1), and prominent and negative Eu anomalies (Eu/Eu* = 0.054, 0.19, 0.025) (Figure 8e). The remaining 17 analyses had concentrations of U and Th ranging from 289 to 1877 ppm and 232 to 1381 ppm, respectively, and Th/U ratios varied from 0.13 to 2.64. They exhibited consistent chondrite-normalized REE patterns with steep HREE slopes ($(Yb/Gd)_N$ = 8.56–53.9), positive Ce anomalies (Ce/Ce* = 1.74–247), and negative Eu anomalies (Eu/Eu* = 0.028–0.19) (Figure 8e).

For sample DG3, three analyses of inherited cores had high concentrations of Th (664, 165, and 1027 ppm) and U (1087, 531, and 1209 ppm) with high Th/U ratios (0.61, 0.31 and 0.85). The REE patterns of inherited cores showed significantly negative Eu anomalies (Eu/Eu* = 0.32, 0.15 and 0.085) (Figure 8f). Sixteen analyses had high Th (663–2455 ppm) and U (311–1330 ppm) contents with widely variable Th/U ratios of 0.57 to 2.81. Chondrite-normalized REE patterns were characterized by steep HREE slopes ($(Yb/Gd)_N$ = 7.60–16.1), positive Ce anomalies (Ce/Ce* = 1.83–39.5), and negative Eu anomalies (Eu/Eu* = 0.038–0.24) (Figure 8f).

5. Discussion

5.1. Significance of Zircon U-Pb Ages and Trace Element Compositions

5.1.1. Nature of the Protoliths

All of the metatexite, diatexite, and biotite monzogranite samples collected from Fuhuling contained inherited zircon. The ages of inherited zircon in granitoid rocks and migmatites is often used to elucidate the age and nature of their sources [59–61]. Concentrations of the REE in zircon provide additional information on their geological significance [56,62]. Inherited zircon from metatexite and diatexite has a large range of Th/U ratios (0.023 to 1.64), and most of them have negative Eu anomalies and steep chondrite-normalized HREE slopes, whereas a few of them have smaller negative Eu anomalies and flatter HREE slopes; these variations may represent different source compositions [63]. This inherited zircon from metatexites and diatexites gives a wide range of ages (*c.* 553–2480 Ma) with a dominant population at *c.* 1000 Ma, which is broadly similar to the age distribution of detrital zircon from basement metasedimentary rocks in the Yunkai region (Figure 9). This suggests that the protoliths of the migmatites are probably metasedimentary rocks. By contrast, inherited zircons from biotite monzogranite show a wide range of ages (*c.* 413–1050 Ma) with a dominant population at *c.* 440 Ma and Th/U ratios greater than 0.1 (0.12–1.00). This zircon has chondrite-normalized REE patterns characterized by steep HREE slopes, significantly negative Eu anomalies, and prominent, positive Ce anomalies, suggesting that they are of magmatic origin [56,57]. This indicates that the migmatites and biotite monzogranites have different sources.

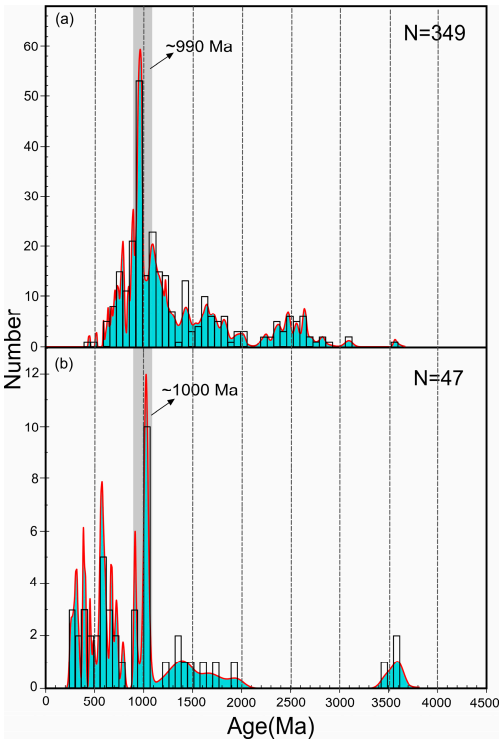

Figure 9. Histograms (blue boxes) and probability distribution functions (red lines) for (**a**) detrital zircons from metasedimentary rocks of Yunkai region and (**b**) inherited zircons from metatexite and diatexite from this study. Data source: Yunkai Group two-mica gneiss and quartz-mica schist [36]; gneiss from Luoding [64]; paragneiss from Xiejie [29]; biotite plagioclase gneiss from Xinyi [65]; and metamorphic feldspar quartz-sandstone from Luola Village, southwest of Luoding, and biotite gneiss from the east of Xinyi [42].

5.1.2. Timing of Crustal Partial Melting in Yunkai Region

In the Fuhuling migmatite complex, metamorphic zircon from metatexite (SPM and FHM) and diatexite (SPMG and FHMG) has both core–rim and homogeneous structures consistent with growth during the crystallization of anatectic melt [54–56,66–68]. Zircon with core–rim structures has cores with oscillatory, planar, or nebulous zoning, which is surrounded by overgrowths with weak oscillatory zoning or no zoning. Homogeneous-structured neoblastic zircon has no cores and weak or no oscillatory zoning. These different internal structures suggest that the metamorphic zircons experienced variable degrees of resorption and recrystallization [54,57,69]. Metamorphic zirconformed by dissolution–reprecipitation also has specific trace element characteristics [54,57,70]. U-Pb ages of homogeneous-structured neoblastic zircons or zircon rims with core–rim structures in samples SPM, FHM, SPMG, and FHMG can be divided into two groups.

One group of 78 analyses yields $^{206}Pb/^{238}U$ ages that range from 431 ± 5 to 454 ± 5 Ma. Compared with inherited zircon in these samples, these analyses also have chondrite-normalized REE patterns with steep HREE slopes, negative Eu anomalies, and prominent, positive Ce anomalies, which are characteristics of zircon crystallized from melt [54,56,70]. Therefore, the weighted mean $^{206}Pb/^{238}U$ ages of 443.3 ±2.7, 44 ±13, 435.4 ± 1.8, and 437.5 ± 3.0 Ma from zircon rims with core–rim structures or homogeneous-structured neoblastic zircon of samples SPM, FHM, SPMG, and FHMG, respectively, are interpreted as the general timings of partial melting. More specifically, because zircon is expected to dissolve during heating and partial melting and grow during cooling and melt crystallization [71–75], these ages most likely represent the timing of neoblastic zircon growth during melt crystallization. The second group of 13 analyses yields $^{206}Pb/^{238}U$ ages of 235 ± 3 to 244 ± 4 Ma and highly variable Th/U ratios (0.02–1.92). Compared with inherited zircon of these samples, chondrite-normalized REE patterns of these analyses are characterized by smaller, negative Eu anomalies, positive Ce anomalies,

and flatter HREE slopes. These arefeatures similar tometamorphic zircon that grows or is recrystallized in the presence of a metamorphic fluid [54,56,70].

Recently, Wang et al. (2013) [31] obtained zircon U-Pb ages from gneissic migmatites from the Longxiu–Yunlu section of the Gaozhou area, and Ke et al. (2018) [42] obtained zircon U-Pb ages from leucosome in migmatites from Luoding, Guangdong, and Xinyi, Guangdong. Both studies documented metamorphic zircon growth mostly in the Early Paleozoic(~440 Ma) and minor growth in the Early Mesozoic(~230 Ma). Wang et al. (2013) [31] suggested that the Early Paleozoicages represent the timing of crustal partial melting, and the Early Mesozoicages may be related to low-temperature metamorphism during Indosinian movement. Ke et al. (2018) [42] interpreted both the Early Paleozoic ages and the Early Mesozoic ages as the timing of melt crystallization and suggestedthat the Yunkai region wasaffected by crustal partial melting in the Early Paleozoic and the Early Mesozoic.

Compared with the zircon analyzed in these studies, the morphology and trace element compositions of zircon from metatexite and diatexite at Fuhuling are similar to that of zircon from gneissic migmatites described byWang et al. (2013) [31] (Figure 10). Geochronology and trace element analysis of zircon from this study indicate that partial melting in the Fuhuling migmatites only occurred in the Early Paleozoic (*c.* 435–444 Ma; Figures 7 and 8), which suggests that crustal partial melting in the Yunkai region occurred during the Early Paleozoic Wuyi–Yunkai orogeny. Early Mesozoic U-Pb ages from zircon rims in the metatexite and diatexite are probably related to fluid-induced dissolution–reprecipitation of zircon, as indicated by their trace element systematics (Figure 8), and not renewed partial melting at this time.

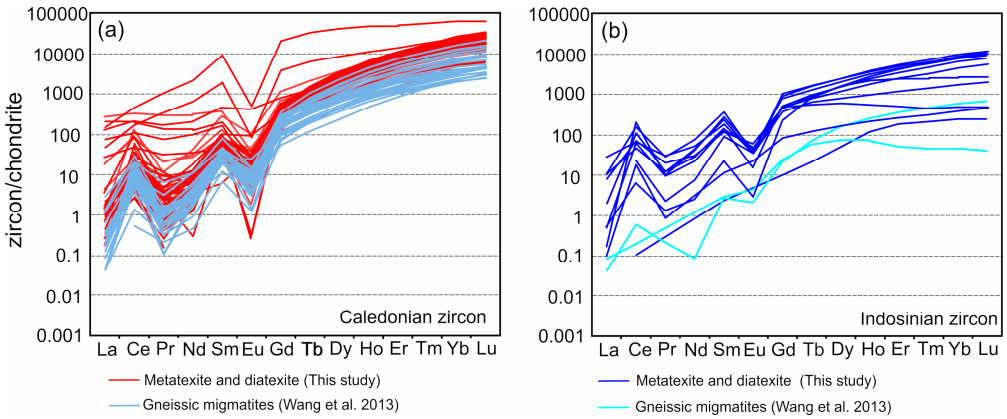

Figure 10. Comparison of chondrite-normalized REE patterns of (**a**) Caledonian zircon and (**b**) Indosinian zircon from this study and from [30]. Chondrite values are from [58].

5.2. Migmatite Morphology and Development

The structures of migmatites formed by partial melting are usually heterogeneous. If migmatites are affected by later high-grade metamorphism, crustal partial melting (anatexis), and even crustal magmatism, then the pre-existing structures formed by partial melting may homogenize or disappear depending on the extent of subsequent melting and the amount of deformation [18–20,25]. Therefore, the macro- and microstructures preserved by migmatites provide important information to determine if they were substantially affected by multiple high-temperature tectonothermal events. Considering that U-Pb zircon ages indicate that the Fuhuling migmatite did not partially melt during the Early Mesozoic, the leucosome–melanosome framework therefore records Early Paleozoic (*c.* 435–444 Ma) melt organization and can be directly linked to deformation during Wuyi–Yunkai orogenesis.

The metatexite–diatexite profile at Fuhuling has a complex geometry at the outcrop scale and exhibitsstructural stratification. Leucosomes in the metatexite are preferentially oriented, whereas leucosome in the diatexite show no preferred orientation (Figure 3). This indicates that the configuration of leucosomes in migmatite changes, and their directionality is weakened during the transition from metatexite to diatexite. These phenomena may be caused by changes in melt

fraction under static conditions [16,25]. Along the profile, the metatexite of layer I and layer II has a typical stromatic structure; the metatexite of layer III contains a large number of flowing folds with different shapes, and the diatexite of layer IV exhibits schlieren and nebulitic structures. All of these are typical mesostructures of migmatite associated with partial melting [20,25,76]. The mesostructures of metatexite and diatexite are distinctly different, which is manifested by the geometry and abundance of leucosome. Leucosome geometry in migmatites is inferred to record evidence of active melt flow, rather than stagnant melt [18,48]. However, leucosomes represent the final vestiges of melt before solidification of the anatectic system. The high abundance of leucosome in some migmatites may reflect melt accumulation rather than a large degree of partial melting of the host. The morphological differences between the metatexite and diatexite layers are a product of the proportion of melt in the system and the amount of pervasive ductile deformation. Metatexite is characterized by the presence of leucosomes parallel to the dominant foliation in the host or superimposed on a transposed inherited compositional layering of sedimentary or magmatic origin [10,18,48]. There is a higher proportion of leucosome in fold hinges than fold limbs, which suggests that these were areas of melt accumulation and probably represent preferred flow pathways for the anatectic melt [10,18,19,48]. The transition from metatexite to diatexite in the Fuhuling migmatites is associated with an increase in the proportion and structural variety of leucosome [10,48]. Diatexite with schlieren or nebulitic structures contains partially resorbed and dismembered paleosome or residuum within a coarser-grained, diffuse leucosome; the preservation of these features suggests that there was no strong pervasive deformation during partial melting [10,19,48]. Diatexite with a schollen structure is characterized by disruption of the more competent layers (typically paleosome or residuum) into "schollen" or "raft" fragments with different orientations, which indicates a more substantial component of ductile deformation compared with the schlieren-bearing diatexite [10,19,48]. The microstructure in migmatites continually readjusts tochanges of partial melting, which reflects information about the crystallization of anatectic melt rather than the melt-producing reactions [5,8,13]. The microstructures in metatexite include fine-grained interstitial quartz, feldspar, and drop-shaped quartz, which probably represent crystallization of the last vestiges of anatectic melt [17,22–24]. Elongated or preferred orientation of feldspar in diatexite suggests a component of magmatic flow while the diatexite was still molten [17,22–24].

5.3. Mechanisms and Causes of Partial Melting at Fuhuling

The Wuyi–Yunkai orogen is an intraplate orogen, and the geodynamic models for its evolution during the Early Paleozoic are still debated [29,31,77]. However, intraplate orogeny probably caused crustal shortening and thickening and resulted in the closure of the pre-existing Nanhua Rift [29,31,77]. The heat needed to initiate and sustain partial melting in the region was probably the result of crustal thickening associated with the Wuyi–Yunkai orogen and concomitant radioactive heat generation from the sedimentary rocks [29,31,77,78] as well as possible residual heat generated by Neoproterozoic plume activity in the region [29,77]. Together, this geodynamic environment of an intraplate orogeny overriding an old plume system is inferred to have led to partial melting of the metasedimentary rocks and some Cathaysian basement rocks [29,31,79].

Partial melting of crustal rocks can proceed through hydrate-breakdown melting, where hydrous minerals are consumed (e.g., biotite, muscovite, amphibole) and anhydrous peritectic minerals (e.g., garnet, orthopyroxene) are generated [80], or through the influx of an externally derived hydrous fluid (e.g., [81,82]). Hydrate-breakdown melting of fertile protoliths can generate up to ~15 vol.% melt through muscovite-breakdown reactions and up to 40 vol.% by biotite-breakdown melting at ultra-high-temperature (>900 °C) conditions [83]. At the same pressure–temperature conditions, fluid-present melting can generate more melt than hydrate-breakdown melting as long as there is a large enough influx of H_2O into the system. In addition, fluid-present partial melting results in a net volume reduction and promotes the retention of melt, as opposed to fluid-absent melting that requires an increase in volume, which is commonly accommodated by melt loss from the system.

Hence, the absence of anhydrous peritectic minerals in the Fuhuling migmatites is inconsistent with fluid-absent, hydrate-breakdown melting.

In general, migmatites in the Wuyi–Yunkai orogen generally contain anhydrous peritectic minerals [31,50], which is consistent with hydrate-breakdown melting. However, the absence of anhydrous peritectic minerals in the Fuhuling migmatites in the Yunkai region is inconsistent with hydrate-breakdown melting. Furthermore, the amount of leucosome in the Fuhuling migmatites is >40 vol.% in many cases (Figure 11); most of this leucosome is inferred to be the product of in situ or in source partial melting. These large volumes of leucosome (i.e., former anatectic melt and entrained minerals) are inconsistent with fluid-absent melting unless ultra-high-temperature conditions were reached (c.f. [84]), these temperatures are not compatible with the abundance of biotite and hornblende in the Fuhuling migmatites. Therefore, migmatites at Fuhuling probably underwent fluid-present melting in the Early Paleozoic, and this mechanism was partly responsible for the morphology of the migmatites.

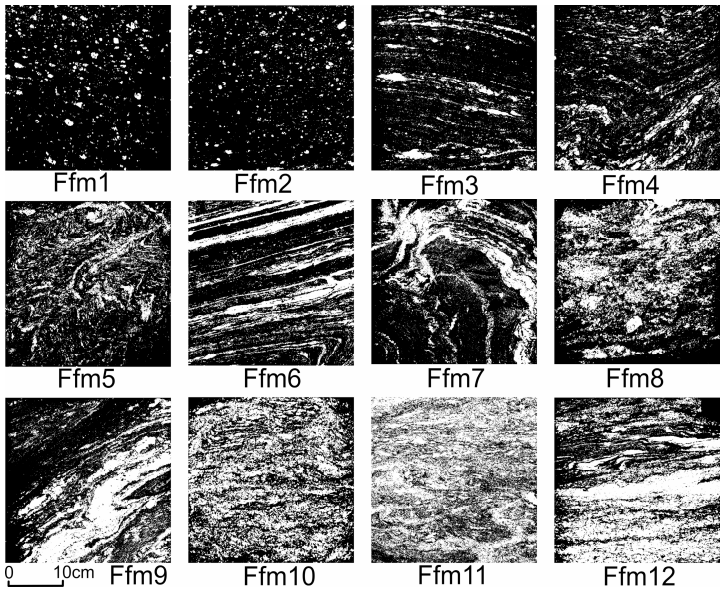

Figure 11. Processed black and white 30 × 30 cm^2 image frames of the metatexite and diatexite from the Fuhuling metatexite–diatexite profile. Positions of the image frames are shown in Figure 2.

5.4. Rheology of the Yunkai Region during the Wuyi–Yunkai Orogeny

Large phanerozoic orogens commonly contain migmatites formed by crustal partial melting, and this process has important implications for the rheology of the crust during orogenesis [3,11,78]. The rheology and strength of partially molten rocks change significantly at two thresholds that are relevant for most migmatite terranes [11,25,85], including the Yunkai region. The first is known as the melt connectivity transition (MCT) [86–89], which is generally thought to occur at 7 vol.% melt in a static system [88]. A second threshold is known as the solid-to-liquid transition (SLT) [88], which is similar to the rheologically critical melt percentage (RCMP), and is characterized by the less-pronounced aggregate strength drop at a melt fraction around 40 vol.% [90–92].

Fuhuling migmatites have variable proportions of leucosome, which is inferred to approximate the variable amount of anatectic melt that was present during orogenesis. Chen et al. (2017) [92] investigated the relationship between aggregate strength versus leucosome fraction in the Fuhuling migmatites and proposed that, in addition to MCT and SLT, there is a third rheological threshold termed the framework-melting transition (FMT). The FMT is characterized by a sharp decrease of aggregate strength at melt fractions of ~21 vol.% and can be interpreted as a transition of the solid framework from compact to fused. An increased proportion of melt results in a progressively weaker crust [93] and has significant effects not only on the nature of partially molten rocks (such as the

Fuhuling migmatites) but also on the crustal-scale tectonic processes [10,19,20] and the evolution of the Wuyi–Yunkai orogen [29–32,39,40].

The structural transition from metatexite to diatexite, such as that observed in the Fuhuling migmatites, is related to the evolution of the rheology of partially molten rocks, which is the result of a complex and dynamic interplay between melt production, melt segregation, melt migration, and melt redistribution [10,19,20]. The amount of melt in migmatitic crust and its role in controlling its rheology can be investigated through macro- and micro-structural analyses based on the distribution and proportion of the melt at the outcrop scale [10,18–20].

To assess the influence of the aggregate strength and melt fraction of the partially melted protolith on the structures of Fuhuling migmatite in the Yunkai region, we quantified leucosome proportions along the metatexite–diatexite transect (Figure 11). The methodology of our approach is the same as described in detail by Zhang et al. (2017) [38] and Chen et al. (2017) [92]. We measured leucosome proportions in each layer of the metatexite–diatexite profile and linked this with the possible rheological transitions controlled by melt fraction (Table S3). Based on the relationship between aggregate strength and melt fraction of the partially melted protolith at Fuhuling [92] and our structural analysis of leucosome networks, we now propose a conceptual model for the variable morphologies observed in the Fuhuling migmatites (Figure 12a–i). This is essential for establishing a link between rheological transitions and crustal partial melting in the Yunkai region during Early Paleozoic Wuyi–Yunkai orogeny.

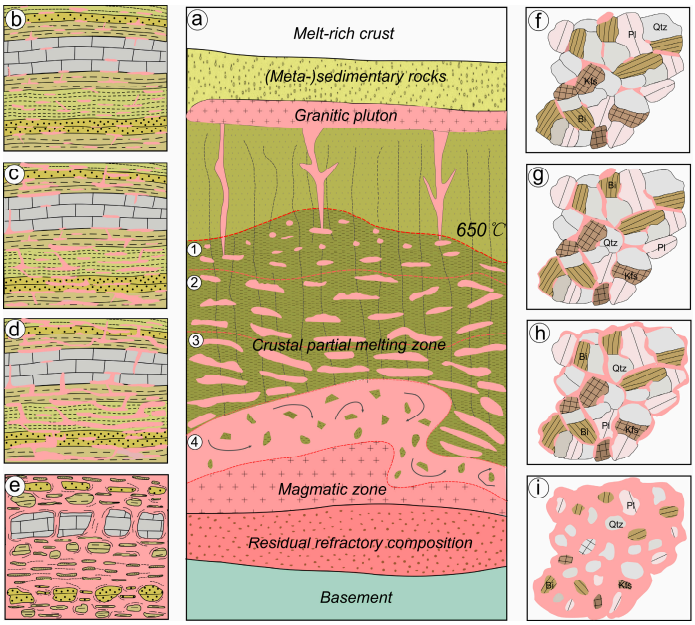

Figure 12. Model of the evolution of the "mixture" composed of partially molten rocks and melt in the Fuhuling during partial melting. (**a**) Partial melting zones of melt-rich crust. Four crustal partial melting zones correspond to the melt fractions of 0–7 vol.%, 7–21 vol.%, 21–40 vol.%, and >40 vol.%. Metatexite formed in crustal zones (1)–(3), while diatexite formed in crustal zone (4), and as the partial melting proceeds, granite will eventually form. The 650 °C isotherm approximates the wet solidus of crustal rocks. (**b**–**e**) Macrostructural sketches of the "mixture" composed of partiallymolten rocks and melt, illustrating the rheological transitions due to changesin the melt fraction when going through the processes of melt production, melt segregation, melt migration, and melt redistribution, which correspond to the melt fractions of 0–7 vol.%, 7–21 vol.%, 21–40 vol.%, and >40 vol.%, respectively (pink = melt, gray or yellow blocks = (meta)sedimentary rocks) (modified after [11,24]). (**f**–**i**) Microstructural sketches illustrating the evolution of the melt/solid two-phase system during partial melting corresponding to the melt fractions of 0–7 vol.%, 7–21 vol.%, 21–40 vol.%, and >40 vol.%, respectively (pink = melt, Qtz = quartz; Kfs = K-feldspar; Pl = plagioclase; Bt = biotite).

At melt fractions <7 vol.%, only a small amount of melt formed at the interstices of mineral grains (Figure 12f). The partially melted protolith remained coherent and banded, and the solid framework and structure of protolith were not compromised (Figure 12b). At the onset of partial melting, the resulting melt formed fine-grained quartzofeldspathic films, which may have a granular macroscopic appearance, along the grain boundaries between the reactant minerals [10,25]. As the fraction of melt in the system increased due to progressive anatexis, the melt formed elongate mottles and intermittent strips (Figure 3a) [25], which are both typical stromatic structures of metatexites [10,25].

At melt fractions between 7 and 21 vol.%, the interstitial melt became connected along grain boundaries (Figure 12g). The partially melted protolith was still coherent and banded (Figure 12c). The melt then organized into thin parallel and laterally continuous leucosomes, which would give the system a layered structure (Figure 3b) [10,25]. This structure is also typical of stromatic metatexites and probably relates to short-range segregation of melt from its residuum in situ or in source [10,19,25].

At melt fractions between 21 and 40 vol.%, the proportion of melt increased due to framework melting but was still restricted within a coherent solid framework (Figure 12h). The partially melted protolith experienced a significant decrease in aggregate strength, coherency compositional banding gradually weakened, and stromatic structures began to deteriorate (Figure 12d). This formed metatexite with folds of a wide range of leucosome orientations as well as melt accumulation in the hinges of folds (Figure 3c,d), suggesting the local migration of melt during folding [19,25].

At melt fractions >40 vol.%, the solid framework was no longer connected (Figure 12i). The coherency and banding of the partially melted protolith were destroyed, and pre-partial melting structures in the migmatites were destroyed (Figure 12e). More competent layers were progressively disrupted into tabular fragments, and typically paleosome and residuum were suspended in the melt forming “schollen” or “rafts” in diatexite (Figure 3f) [25]. Elongate or preferentially oriented quartz, plagioclase, and biotite are common in diatexite due to magmatic flow (Figure 4f,h) [20,25]. These characteristics indicate that the continuity of the solid framework was lost [10,88].

If partial melting proceeds and melt cannot be effectively drained, the accumulation of melt and settling of partiallymolten residuum will lead to the transition from a “mixture”—composed of the partially molten protolith and melt—to magmas that may ascend to form granite plutons [11] or remain in the anatectic crust. In the Yunkai region, Early Paleozoic migmatites and granites are considered to have a genetic link because of the synchronicity between crustal partial melting and magmatism [30–32]. Current geodynamic models of the Wuyi–Yunkai orogeny include crustal partial melting (anatexis) during the Early Paleozoic [29,31,77], but the rheological effects of a melt-rich crust on this intraplate orogen are unclear.During orogenesis, partial melting of the crust is heterogeneous given the variable fertilities of different lithologies [94]. If the crust incorporates large quantities of fertile (meta)sedimentary rocks, it may be able to generate voluminous anatectic melt [15,85]. In contrast to the fluid-present melting documented at Fuhuling, anhydrous peritectic minerals associated with higher-temperature hydrate-breakdown melting are present elsewhere in the Yunkai region [31]. The preservation of anhydrous peritectic minerals in anatectic rocks requires the loss of anatectic melt [95] and leaves behind a more refractory residue that is expected to be stronger than the unmelted protolith [96]. This contrasts with the large amount of leucosome observed at Fuhuling, which suggests substantial melt retention and possible melt accumulation. Consequently, the Yunkai region may represent a section through a heterogeneous crust with both melt-rich (weak) and melt-poor (strong) horizons, and this suggests that partial melting of the crust and the amount of melt in different crustal horizons was heterogeneous during the Wuyi–Yunkai orogeny (Figure 13).

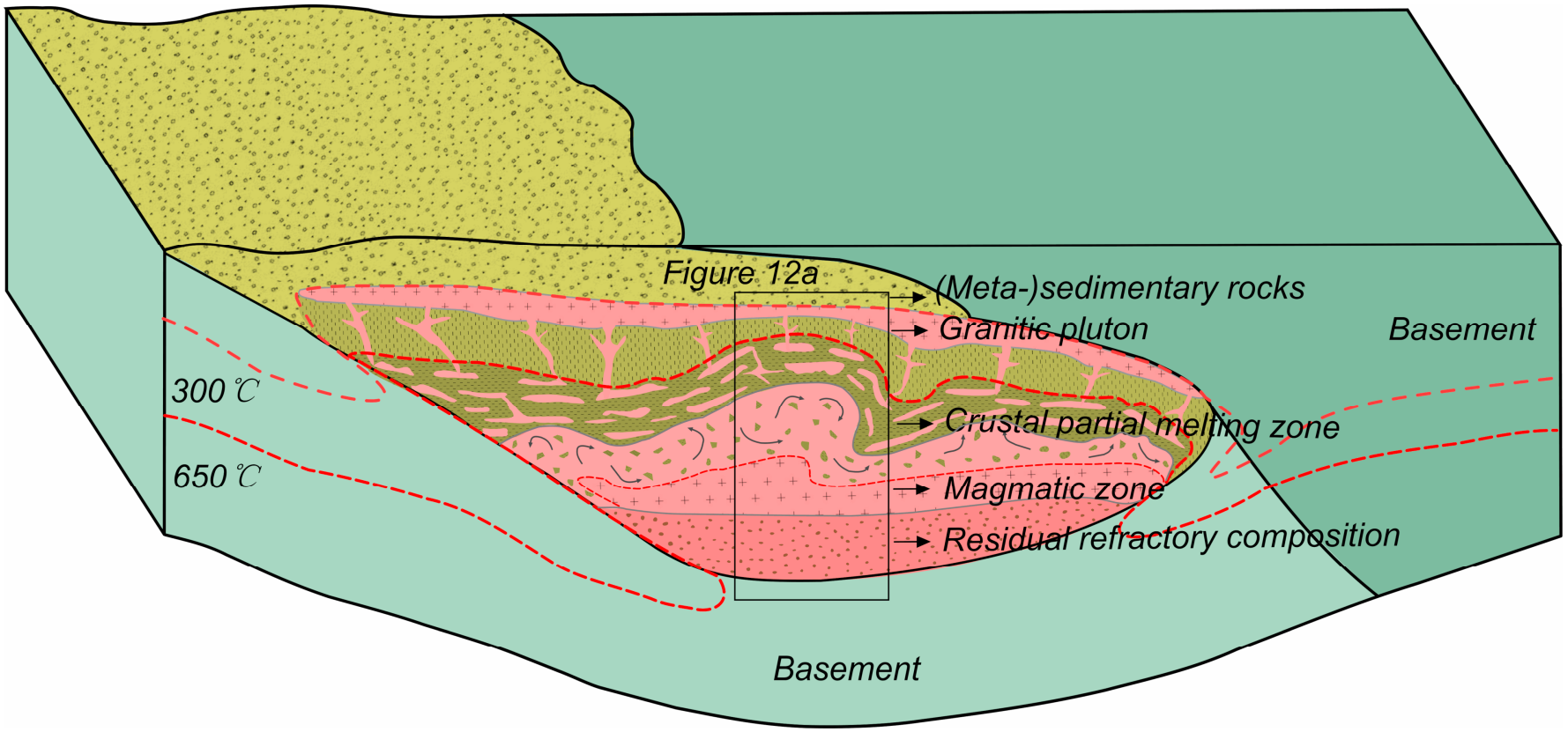

Figure 13. Conceptual model for crustal partial melting in the Yunkai region during the Early Paleozoic Wuyi–Yunkai orogen. The pink and the red thick dashed lines represent the isotherms of 300 °C and 650 °C, respectively.

Spatial analysis of leucosomes at Fuhuling implies that a large proportion of melt remained in the deep crust, which is evidenced by the presence of diatexites and metatexites with high melt fractions at Fuhuling. Melt retention in the middle to deep crust has also been proposed in other migmatite terranes [26,46], but this contrasts with the general view that the continental crust is differentiated due to the ascent of granitic materials in dykes that have no or minimal interaction with the surrounding rock during ascent (c.f. [80]). Such crustal-scale mass transfer is facilitated by buoyancy-driven magma ascent [97,98], and the heat advected with migrating melt may promote amplification of thermal anti form, extending the zone of partial melting to shallower crust that weakens the crust during orogeny [13,85,99]. The buoyancy contrast between metatexite and relatively melt-rich diatexite may also promote the buoyant rise of partially molten diatexite, which is a common inference from gneiss domes [99–101]. The Fuhuling diatexites have complex morphologies with leucosomes that lack preferred orientations, which contrasts with the preferred orientation of leucosomes in the overlying metatexites. This suggests that the loss of cohesion at high melt fractions in the diatexites possibly coupled with buoyancy-driven uplift were important factors in the heterogeneity of the leucosomes in diatexites compared to leucosome in the metatexites. Overall, the Fuhuling migmatites show rheological transitions caused by a change in melt fraction. Given that structural processes are expected to be scale-invariant in migmatite terranes [26,102], the rheological transitions documented in the Fuhuling migmatites are probably reflective of the crustal-scale rheological heterogeneity that existed in the Yunkai region during the Early Paleozoic Wuyi–Yunkai orogen (Figure 13). Consequently, the high melt fractions inferred in the deep crust may have played a key role in facilitating orogenic collapse in the Yunkai region in the Early Paleozoic [79].

6. Conclusions

1. Zircon U-Pb geochronology and trace element analysis indicate that biotite monzogranites are not derived from the migmatites at Fuhuling. Partial melting at Fuhuling in the Yunkai region occurred during Early Paleozoic Wuyi–Yunkai orogenesis. Minor zircon dissolution–reprecipitation in the Indosinian was probably related to lower-temperature metamorphism.

2. Migmatites at Fuhuling were produced by fluid-present melting, have morphologies ranging from metatexite to diatexites, and were not affected by deformation associated with Indosinian movement.

3. Morphological differences across the metatexite–diatexite transition in the Fuhuling migmatites may have been caused by a change in melt connectivity and continuity of the solid framework because there were variable proportions of solid and melt during partial melting and deformation.

4. The abundance of leucosome in the Fuhuling migmatites suggests that it acted as a melt-rich and buoyant horizon. The rheological transitions documented in the Fuhuling migmatites may be analogous with the rheological transitions that operated the deep melt-rich crust after crustal thickening associated with the Early Paleozoic Wuyi–Yunkai orogenesis.

Supplementary Materials: The following are available online at http://www.mdpi.com/2075-163X/9/10/621/s1, Table S1: Zircon U-Pb data of the metatexite, diatexite and biotite monzogranite from Fuhuling in Yunkai region. Table S2: Zircon trace element of the metatexite, diatexite and biotite monzogranite from Fuhuling in Yunkai Region. Table S3: Leucosome proportion of metatexite and diatexite in Fuhuling profile.

Author Contributions: Conceptualization, J.Z. and W.L.; Methodology and formal analysis, J.Z., Q.X., Y.W. and Z.Z.; Data curation, R.D., G.T. and H.L.; Investigation, J.Z., R.D. and W.L.; Writing—original draft preparation, J.Z. and R.S.; Writing—review and editing, C.Y. and W.L.; Funding Acquisition, W.L.

Funding: This research was funded by the National Natural Science Foundation of China [grant numbers 41972049, 41372223, 41472054, 41977231, 41502277 and 41102131]; Guangzhou Science Technology and Innovation Commission Project [grant number 201904010138]; the China State Scholarship Fund of visiting scholar [grant number 20170638507]; the Special Fund for Basic Scientific Research of Central Colleges, Chang'an University [grant numbers 300102268502, 300102269504]; the Fund of Key Laboratory of Mine Geological Hazards Mechanism and Control [grant number 2017KF06]; Research grant of State Key Laboratory of Isotope Geochemistry, Guangzhou Institute of Geochemistry, Chinese Academy of Sciences [grant number SKLaBIG-KF-18-11]; National Higher Education Quality Monitoring Data Center of Sun Yat-Sen University [grant number G1914];

and SYSU Course Construction Project for Postgraduates [grant number 201922]. The APC was funded by National Natural Science Foundation of China [grant number 41972049].

Acknowledgments: Our deepest gratitude goes to Guoneng Chen for his critical comments on this research. We thank Zhen Chen, Heping Zou, and Feng Lou for helpful suggestions as well as students Haihua Huang and Wei Qiu for assistance during field work. We are grateful to two anonymous reviewers for their constructive comments and suggestions.

Conflicts of Interest: The authors declare there is no conflict of interest regarding the publication of this paper.

References

1. Brown, M. The generation, segregation, ascent and emplacement of granite magma: The migmatite-to-crusstally-derived granite connection in thickened orogens. *Earth Sci. Rev.* **1994**, *36*, 83–130. [CrossRef]
2. Nelson, K.D.; Zhao, W.; Brown, L.D.; Kuo, J.; Che, J.; Liu, X.W.; Klemperer, S.L.; Makovsky, Y.; Meissner, R.; Mechie, J.; et al. Partially molten middle crust beneath Southern Tibet: Synthesis of project INDEPTH results. *Science* **1996**, *274*, 1684–1688. [CrossRef] [PubMed]
3. Vanderhaeghe, O.; Teyssier, C. Partial melting and flow of orogens. *Tectonophysics* **2001**, *342*, 451–472. [CrossRef]
4. Groome, W.G.; Koons, P.O.; Johnson, S.E. Metamorphism, transient mid-crustal rheology, strain localization and the exhumation of high-grade metamorphic rocks. *Tectonics* **2008**, *27*. [CrossRef]
5. Sawyer, E.W.; Cesare, B.; Brown, M. When the continental crust melts. *Elements* **2011**, *7*, 229–234. [CrossRef]
6. Hollister, L.S. The role of melt in the uplift and exhumation of orogenic belts. *Chem. Geol.* **1993**, *108*, 31–48. [CrossRef]
7. Brown, M. Crustal melting and melt extraction, ascent and emplacement inorogens: Mechanisms and consequences. *J. Geol. Soc.* **2007**, *164*, 709–730. [CrossRef]
8. Sawyer, E.W. Melt segregation in the continental crust. *Geology* **1994**, *22*, 1019–1022. [CrossRef]
9. Wickham, S.M. The segregation and emplacement of granitic magmas. *J. Geol. Soc.* **1987**, *144*, 281–297. [CrossRef]
10. Vanderhaeghe, O. Melt segragation, pervasive melt migration and magma mobility in the continental crust: The structural record from pores to orogens. *Phys. Chem. Earth Part A Solid Earth Geod.* **2001**, *26*, 213–223. [CrossRef]
11. Vanderhaeghe, O. Migmatites, granites and orogeny: Flow modes of partially-molten rocks and magmas associated with melt/solid segregation in orogenic belts. *Tectonophysics* **2009**, *477*, 119–134. [CrossRef]
12. Mclellan, E.L. Deformational behaviour of migmatites and problems of structural analysis in migmatite terrains. *Geol. Mag.* **1984**, *121*, 339–345. [CrossRef]
13. Brown, M.; Averkin, Y.A.; McLellan, E.L.; Sawyer, E.W. Melt segregation in migmatites. *J. Geophys. Res.* **1995**, *100*, 15655–15679. [CrossRef]
14. Brown, M. The definition of metatexis, diatexis and migmatite. *Proc. Geologists' Assoc.* **1973**, *84*, 371–382. [CrossRef]
15. Sawyer, E.W. Formation and evolution of granite magmas during crustal reworking: The significance of diatexites. *J. Petrol.* **1998**, *39*, 1147–1167. [CrossRef]
16. White, R.W.; Pomroy, N.E.; Powell, R. An in situ metatexite-diatexite transition in upper amphibolite facies rocks from Broken Hill, Australia. *J. Metamorph. Geol.* **2005**, *23*, 579–602. [CrossRef]
17. Holness, M.B. Working with migmatites: Decoding migmatite microstructures. In *Working with Migmatites*; Sawyer, E.W., Brown, M., Eds.; Short Course Series; Mineralogical Association of Canada: Quebec, QC, Canada, 2008; Volume 38, pp. 57–76.
18. Kruckenberg, S.C.; Vanderhaeghe, O.; Ferré, E.C.; Teyssier, C.; Whitney, D.L. Flow of partially molten crust and the internal dynamics of a migmatite dome, Naxos, Greece. *Tectonics* **2011**, *30*, 445–455. [CrossRef]
19. Weinberg, R.F.; Mark, G. Magma migration, folding, and disaggregation of migmatites in the Karakoram shear zone, Ladakh, NW India. *Geol. Soc. Am. Bull.* **2008**, *120*, 994–1009. [CrossRef]
20. Viegas, L.G.F.; Archanjo, C.J.; Vauchez, A. Fabrics of migmatites and the relationships between partial melting and deformation in high-grade transpressional shear zones: The Espinho Branco anatexite (BorboremaProvince, NE Brazil). *J. Struct. Geol.* **2013**, *48*, 45–56. [CrossRef]

21. Stipska, P.; Schulmann, K.; Powell, R. Contrasting metamorphic histories of lenses of high-pressure rocks and host migmatites with a flat orogenic fabric (Bohemian Massif, Czech Republic): A result of tectonic mixing within horizontal crustal flow? *J. Metamorph. Geol.* **2008**, *26*, 623–646.
22. Vernon, R.H. Review of microstructural evidence of magmatic and solid-state flow. *Vis. Geosci.* **2000**, *5*, 1–23. [CrossRef]
23. Rosenberg, C.L. Deformation of partially molten granite: A review and comparison of experimental and natural case studies. *Int. J. Earth Sci.* **2001**, *90*, 60–76. [CrossRef]
24. Saki, A. Migmatite microstructures and partial melting of Hamadan metapelitic rocks, Alvand contact aureole, western Iran. *Int. Geol. Rev.* **2012**, *54*, 1229–1240. [CrossRef]
25. Sawyer, E.W. Working with migmatites: Nomenclature for the constituent parts. In *Working with Migmatites*; Sawyer, E.W., Brown, M., Eds.; Short Course Series; Mineralogical Association of Canada: Quebec, QC, Canada, 2008; Volume 38, pp. 1–28.
26. Yakymchuk, C.; Brown, M.; Ivanic, T.J.; Korhonen, F.J. Leucosome distribution in migmatitic paragneisses and orthogneisses: A record of self-organized melt migration and entrapment in a heterogeneous partially-molten crust. *Tectonophysics* **2013**, *603*, 136–154. [CrossRef]
27. Brown, M. Introduction to a virtual special issue on crustal melting. *J. Metamorph. Geol.* **2012**, *30*, 453–456. [CrossRef]
28. Searle, M. Crustal melting, ductile flow, and deformation in mountain belts: Cause and effect relationships. *Lithosphere* **2013**, *5*, 547–554. [CrossRef]
29. Li, Z.X.; Li, X.H.; Wartho, J.A.; Clark, C.; Li, W.X.; Zhang, C.L.; Bao, C.M. Magmatic and metamorphic events during the Early Paleozoic Wuyi–Yunkai Orogeny, southeastern South China: New age constraints and P–T conditions. *GSA Bull.* **2010**, *122*, 772–793. [CrossRef]
30. Wang, Y.J.; Zhang, A.M.; Fan, W.M.; Zhao, G.C.; Zhang, G.W.; Zhang, Y.Z.; Zhang, F.F.; Li, S.H. Kwangsian crustal anatexis within theeastern South China Block: Geochemical, zircon U-Pb geochronological and Hf isotopic finger prints from the gneissoid granites of Wugong and Wuyi-Yunkai Domains. *Lithos* **2011**, *127*, 239–260. [CrossRef]
31. Wang, D.; Zheng, J.; Ma, Q.; Griffin, W.L.; Zhao, H.; Wong, J. Early Paleozoic crustal anatexis in the intraplate Wuyi-Yunkai orogen, South China. *Lithos* **2013**, *175*, 124–145. [CrossRef]
32. Liu, R.; Zhou, H.; Zhang, L.; Zhong, Z.Q.; Zeng, W.; Xiang, H.; Jin, S.; Lu, X.Q.; Li, C.Z. Zircon U-Pb ages and Hf isotope compositions of the Mayuan migmatite complex, NWFujian province, Southeast China: Constraints on the timing and nature of a regional tectonothermal event associated with the Caledonian orogeny. *Lithos* **2010**, *119*, 163–180. [CrossRef]
33. Peng, S.P.; Peng, S.M.; Shao, J.G. Microscopic-ultra microscopic analysis of different deformational phases in Yunkai area and its significance. *Guangdong Geol.* **1995**, *10*, 17–24. (In Chinese with English abstract)
34. Wang, Y.X.; Zhao, Z.H.; Bao, Z.W.; Li, X.H. Geochemistry of granitoids from Zhejiang Province and crustal evolution-II. Proterozoic granitoids. *Geochimica* **1997**, *26*, 57–68. (In Chinese with English abstract)
35. Shen, W.Z.; Ling, H.F.; Li, W.X.; Huang, X.L.; Wang, D.Z. Study on the Nd-Sr isotopic compositions of granitoids in SE China. *Geol. J. China Univ.* **1999**, *5*, 22–32. (In Chinese with English abstract)
36. Zheng, Y.F.; Zhang, S.B. Formation and evolution of Precambrian continental crust in South China. *Chin. Sci. Bull.* **2007**, *52*, 1–12. [CrossRef]
37. Wan, Y.S.; Liu, D.Y.; Wilde, S.A.; Cao, J.J.; Chen, B.; Dong, C.Y.; Song, B.; Du, L.L. Evolution of the Yunkai terrane, South China: Evidence from SHRIMP zircon U-Pb dating, geochemistry and Nd isotope. *J. Asian Earth Sci.* **2010**, *37*, 140–153. [CrossRef]
38. Zhang, J.H.; Chen, Z.; Chen, G.N.; Ding, R.X.; Peng, Z.L. Studies of formation temperature of Caledonian migmatite-granite at the Fuhuling area of the southern Qinzhou-Hangzhou zone, South China. *Acta Petrol. Sin.* **2017**, *33*, 887–895, (In Chinese with English abstract).
39. Charvet, J.; Shu, L.S.; Shi, Y.S.; Guo, L.Z.; Faure, M. The building of South China: Collision of Yangzi and Cathaysia Blocks, problems and tentative answers. *J. Southeast Asian Earth Sci.* **1996**, *13*, 223–235. [CrossRef]
40. Wang, Y.J.; Fan, W.; Zhang, G.; Zhang, Y. Phanerozoic tectonics of the south china block: Key observations and controversies. *Gondwana Res.* **2013**, *23*, 1273–1305. [CrossRef]
41. Lin, W.; Wang, Q.C.; Chen, K. Phanerozoic tectonics of South China Block: New insights from the polyphase deformation in the Yunkai massif. *Tectonics* **2008**, *27*. [CrossRef]

42. Ke, X.Z.; Zhou, D.; Long, W.G.; Wang, J.; Xu, D.M.; Tian, Y.; Jin, W. Indosinian metamorphism and anatexis in Yunkai Massif: Evidences from zircon geochronology and Hf isotopes of migmatites and gneisses. *Earth Sci.* **2018**, *8*. (In Chinese with English abstract) [CrossRef]
43. Zhou, X.Y.; Yu, J.H.; Wang, L.J.; Shen, L.W.; Zhang, C.H. Compositions andformation of the basement metamorphicrocks in Yunkai terrane, western Guangdong Province, South China. *Acta Petrol. Sin.* **2015**, *31*, 855–882. (In Chinese with English abstract)
44. RGMRGD. *Regional Geological Mapping and Report of Guangdong Province-Yangjiang Sheet*; Scale 1:200,000; Institute of Geoscience, Ministry of Geology: Beijing, China, 1964. (In Chinese)
45. Bureau of Geology and Mineral Resources of Guangdong Province (BGMRGD). *Regional Geology of the Guangdong Province*; Geological Publishing House: Beijing, China, 1988. (In Chinese with English abstract)
46. Wu, Y.B.; Zheng, Y.F.; Zhang, S.B.; Zhao, Z.F.; Wu, F.Y.; Liu, X.M. Zircon U–Pb ages and Hf isotope compositions of migmatite from the North Dabie terrane in China: Constraints on partial melting. *J. Metamorph. Geol.* **2010**, *25*, 991–1009. [CrossRef]
47. Yao, J.; Shu, L.S.; Cawood, P.A.; Li, J.Y. Constraining timing and tectonic implications of Neoproterozoic metamorphic event in the Cathaysia block, South China. *Precambrian Res.* **2017**, *293*, 1–12. [CrossRef]
48. Morfin, S.; Sawyer, E.W.; Bandyayera, D. Largevolumes of anatectic melt retained in granulite facies migmatites: An injection complex in northern Quebec. *Lithos* **2013**, *168–169*, 200–218. [CrossRef]
49. Holness, M.B.; Clemens, J.D. Partial melting of the Appin quartzite driven by fracture controlled H_2O infiltration in the aureole of the Ballachulish Igneous Complex, Scottish Highlands. *Contrib. Mineral. Petrol.* **1999**, *136*, 154–168. [CrossRef]
50. Liu, R.; Zhang, L.; Zhou, H.W.; Zhong, Z.Q.; Zeng, W.; Xiang, H.; Jin, S.; Lu, X.Q.; Li, C.Z. Petrogenesis of the Caledonian migmatitesa and related granites in northwestern Fujian province, South China: Syn-deformation crustal anatexis. *Acta Petrol. Sin.* **2008**, *24*, 1205–1222.
51. Liu, Y.S.; Gao, S.; Hu, Z.C.; Gao, C.G.; Zong, K.Q.; Wang, D.B. Continental and oceanic crust recycling-induced melt-peridotite interactions in the Trans-North China orogen: U-Pb dating, Hf isotopes and trace elements in zircons from mantle xenoliths. *J. Petrol.* **2010**, *51*, 537–571. [CrossRef]
52. Andersen, T. Correction of common lead in U-Pb analyses that do not report ^{204}Pb. *Chem. Geol.* **2002**, *192*, 59–79. [CrossRef]
53. Ludwig, K.R. *ISOPLOT 3.00, A Geochronology Toolkit for Microsoft Excel*; Berkeley Geochronological Center Special Publication: Berkeley, CA, USA, 2003.
54. Hoskin, P.W.O.; Black, L. Metamorphic zircon formation by solid-state recrystallization of protolith igneous zircon. *J. Metamorph. Geol.* **2000**, *18*, 423–439. [CrossRef]
55. Corfu, F.; Hanchar, J.M.; Hoskin, P.W.O.; Kinny, P.D. Atlas of zircon textures. *Rev. Mineral. Geochem.* **2003**, *53*, 469–500. [CrossRef]
56. Hoskin, P.W.O.; Schaltegger, U. The Composition of zircon and igneous and metamorphic petrogenesis. *Rev. Mineral. Geochem.* **2003**, *53*, 27–62. [CrossRef]
57. Hoskin, P.W.O.; Ireland, T.R. Rare earth element chemistry of zircon and its use as a provenance indicator. *Geology* **2000**, *28*, 627. [CrossRef]
58. Mcdonough, W.F.; Sun, S.S. The composition of the earth. *Chem. Geol.* **1995**, *120*, 223–253. [CrossRef]
59. Watson, E.B.; Harrison, T.M. Zircon saturation revisited: Temperature and composition effects in a variety of crustal magma types. *Earth Planet. Sci. Lett.* **1983**, *64*, 295–304. [CrossRef]
60. Paterson, B.A.; Stephens, W.E.; Rogers, G.; Williams, I.S.; Hinton, R.W.; Herd, D.A. The nature of zircon inheritance in two granite plutons. *Trans. R. Soc. Edinb. Earth Sci.* **1992**, *83*, 459–471.
61. Clemens, J.D. S-type granitic magmas-petrogenetic issues, models and evidence. *Earth Sci. Rev.* **2003**, *61*, 1–18. [CrossRef]
62. Zeck, H.P.; Williams, I.S. Inherited and magmatic zircon from Neogene Hoyazo cordierite dacite, SE Spain-anatectic source rock provenance and magmatic evolution. *J. Petrol.* **2002**, *43*, 1089–1104. [CrossRef]
63. Whitehouse, M.J.; Platt, J. Dating high-grade metamorphism-constraints from rare-earth elements in zircon and garnet. *Contrib. Mineral. Petrol.* **2003**, *145*, 61–74. [CrossRef]
64. Yu, J.H.; O'Reilly, S.Y.; Wang, L.; Griffin, W.L.; Zhou, M.F.; Zhang, M.; Shu, L. Components and episodic growth of Precambrian crust in the Cathaysia Block, South China: Evidence from U–Pb ages and Hf isotopes of zircons in Neoproterozoic sediments. *Precambrian Res.* **2010**, *181*, 97–114. [CrossRef]

65. Wang, L.; Long, W.G.; Xu, D.M.; Xu, W.C.; Zhou, D.; Jin, X.B.; Huang, H.; Zhang, K. Zircon U-Pb geochronology of metamorphic basement in Yunkai area and its implications on the Grenvillian event in the Cathaysia Block. *Earth Sci. Front.* **2015**, *22*, 25–40. (In Chinese with English abstract)
66. Johannes, W. Migmatites: The significance of experimental studies for the formation of migmatites. In *Migmatites*; Ashworth, J.R., Ed.; Springer: Boston, MA, USA, 1985; pp. 36–85.
67. Schaltegger, U.; Fanning, C.M.; Günther, D.; Maurin, J.C.; Schulmann, K.; Gebauer, D. Growth, annealing and recrystallization of zircon and preservation of monazite in high-grade metamorphism: Conventional and in-situ U-Pb isotope, Cathodoluminescence and microchemical evidence. *Contrib. Mineral. Petrol.* **1999**, *134*, 186–201. [CrossRef]
68. Harley, S.L.; Kelly, N.M.; Moller, A. Zircon Behaviour and the Thermal Histories of Mountain Chains. *Elements* **2007**, *3*, 25–30. [CrossRef]
69. Foster, D.A.; Schafer, C.; Fanning, C.M.; Hyndman, D.W. Relationships between crustal partial melting, plutonism, orogeny, and exhumation: Idaho-Bitterroot batholith. *Tectonophysics* **2001**, *342*, 313–350. [CrossRef]
70. Rubatto, D. Zircon trace element geochemistry: Partitioning with garnet and the link between U-Pb ages and metamorphism. *Chem. Geol.* **2002**, *184*, 123–138. [CrossRef]
71. Kelsey, D.E.; Clark, C.; Hand, M. Thermobarometric modelling of zircon and monazite growth in melt-bearing systems: Examples using model metapelitic and metapsammitic granulites. *J. Metamorph. Geol.* **2008**, *26*, 199–212. [CrossRef]
72. Yakymchuk, C.; Brown, M. Behaviour of zircon and monazite during crustal melting. *J. Geol. Soc. Lond.* **2014**, *171*, 465–479. [CrossRef]
73. Kohn, M.J.; Corrie, S.L.; Markley, C. The fall and rise of metamorphic zircon. *Am. Mineral.* **2015**, *100*, 897–908. [CrossRef]
74. Yakymchuk, C.; Clark, C.; White, R.W. Phase relations, reaction sequences and petrochronology. *Rev. Mineral. Geochem.* **2017**, *83*, 13–53. [CrossRef]
75. Yakymchuk, C.; Kirkland, C.L.; Clark, C. Th/U ratios in metamorphic zircon. *J. Metamorph. Geol.* **2018**, *36*, 715–737. [CrossRef]
76. Cavalcante, G.C.G.; Viegas, G.; Archanjo, C.J.; Silva, M.E.D. The influence of partial melting and melt migration on the rheology of the continental crust. *J. Geodyn.* **2016**, *101*, 186–199. [CrossRef]
77. Charvet, J. The Neoproterozoic–Early paleozoic tectonic evolution of the south china block: An overview. *J. Asian Earth Sci.* **2013**, *74*, 198–209. [CrossRef]
78. Wang, Y.J.; Fan, W.M.; Zhao, G.C.; Ji, S.C.; Peng, T.P. Zircon U–Pb geochronology of gneissic rocks in the Yunkai Massif and its implications on the Caledonian event in the South China Block. *Gondwana Res.* **2007**, *12*, 404–416. [CrossRef]
79. Yao, W.H.; Li, Z.X.; Li, W.X.; Li, W.X.; Wang, X.C.; Li, X.H.; Yang, J.H. Post-kinematic lithospheric delamination of the Wuyi–Yunkai orogen in South China: evidence from ca. 435 Ma high-Mg basalts. *Lithos* **2012**, *154*, 115–129. [CrossRef]
80. Brown, M. Granite: From genesis to emplacement. *Geol. Soc. Am. Bull.* **2013**, *125*, 1079–1113. [CrossRef]
81. Weinberg, R.F.; Hasalová, P. Water-fluxed melting of the continental crust: A review. *Lithos* **2015**, *212–215*, 158–188. [CrossRef]
82. Yakymchuk, C.; Zhao, W.; Wan, Y.; Lin, S.; Longstaffe, F.J. Fluid-present anatexis of Neoarchean tonalite and amphibolite in the Western Shandong Province. *Lithos* **2019**, *326*, 110–124. [CrossRef]
83. Yakymchuk, C.; Brown, M. Consequences of open-system melting in tectonics. *J. Geol. Soc.* **2014**, *171*, 21–40. [CrossRef]
84. Kelsey, D.E.; Hand, M. On ultrahigh temperature crustal metamorphism: Phase equilibria, trace element thermometry, bulk composition, heat sources, timescales and tectonic settings. *Geosci. Front.* **2015**, *6*, 311–356. [CrossRef]
85. Brown, M. Orogeny, migmatites and leucogranites: A review. *J. Earth Planet. Sci.* **2001**, *110*, 313–336. [CrossRef]
86. Kriegsman, L.M. Partial melting, partial melt extraction and partial back reaction in anatectic migmatites. *Lithos* **2001**, *56*, 75–96. [CrossRef]
87. Rosenberg, C.L.; Riller, U. Partial-melt topology in statically and dynamically recrystallized granite. *Geology* **2000**, *28*, 7–10. [CrossRef]

88. Rosenberg, C.L.; Handy, M.R. Experimental deformation of partially melted granite revisited: Implications for the continental crust. *J. Metamorph. Geol.* **2005**, *23*, 19–28. [CrossRef]
89. Soesoo, A.; Bons, P.D. From Migmatites to plutons: Power law relationships in the evolution of magmatic bodies. *Pure Appl. Geophys.* **2014**, *172*, 1787–1801. [CrossRef]
90. Arzi, A.A. Critical phenomena in the rheology of partially melted rocks. *Tectonophysics* **1978**, *44*, 173–184. [CrossRef]
91. Takeda, Y.; Obata, M. Some comments on the rheologically critical melt percentage. *J. Struct. Geol.* **2003**, *25*, 813–818. [CrossRef]
92. Chen, Z.; Liu, Y.J.; Chen, G.N.; Peng, Z.L. Rheological transitions in progressive melting of rock and their geological constraints from the Fuhu metatexite-diatexite profile in Guangdong province, SE China. *J. Asian Earth Sci.* **2017**, *139*, 192–201. [CrossRef]
93. Jamieson, R.A.; Unsworth, M.J.; Harris, N.B.; Rosenberg, C.L.; Schulmann, K. Crustal Melting and the Flow of Mountains. *Elements* **2011**, *7*, 253–260. [CrossRef]
94. Clemens, J.D. Melting of the continental crust: Fluid regimes, melting reactions, and source-rock fertility. In *Evolution and Differentiation of the Continental Crust*; Brown, M., Rushmer, T., Eds.; Cambridge University Press: Cambridge, UK, 2006; pp. 297–331.
95. White, R.W. Working with migmatites: Insights gained from the petrological modelling of migmatites: Particular reference to mineral assemblages and common replacement textures. In *Working with Migmatites*; Sawyer, E.W., Brown, M., Eds.; Short Course Series; Mineralogical Association of Canada: Quebec, QC, Canada, 2008; Volume 38, pp. 77–96.
96. Diener, J.F.A.; Fagereng, Å. The influence of melting and melt drainage on crustal rheology during orogenesis. *J. Geophys. Res. Solid Earth.* **2015**, *119*, 6193–6210. [CrossRef]
97. Olsen, S.N.; Marsh, B.D.; Baumgartner, L. Modelling mid-crustal migmatite terrains as feeder zones for granite plutons: The competing dynamics of melt transfer by bulk versus porous flow. *Trans. R. Soc. Edinb. Earth Sci.* **2004**, *95*, 49–58.
98. Barraud, J.; Véronique, G.; Allemand, P.; Grandjean, P. Analogue models of melt-flow networks in folding migmatites. *J. Struct. Geol.* **2004**, *26*, 307–324. [CrossRef]
99. Kruckenberg, S.C. The Dynamics of Migmatite Domes in Extending Orogens. Ph.D. Thesis, University of Minnesota, Minneapolis, MN, USA, 2009.
100. Rey, P.; Vanderhaeghe, O.; Teyssier, C. Gravitational collapse of the continental crust; definition, regimes and modes. *Tectonophysics* **2001**, *342*, 435–449. [CrossRef]
101. Whitney, D.L.; Teyssier, C.; Vanderhaeghe, O. Gneiss domes and crustal flow. In *Gneiss Domes in Orogeny*; Whitney, D.L., Ed.; Paper 380; Geological Society of America: Boulder, CO, USA, 2004; pp. 15–33.
102. Marchildon, N.; Brown, M. Spatial distribution of melt-bearing structures in anatectic rocks from Southern Brittany, France: Implications for melt transfer at grain-to orogen-scale. *Tectonophysics* **2003**, *364*, 215–235. [CrossRef]